CHALMERS

Ringhals Diagnostics and Monitoring, Annual Research Report 2019-20

I. PÁZSIT
L.A. TORRES
C. MONTALVO
L. NAGY
M. SZIEBERTH
G. KLUJBER
T. MISAWA
Y. KITAMURA
H. NYLÉN

Nuclear Engineering Group
Division of Subatomic and Plasma Physics
CHALMERS UNIVERSITY OF TECHNOLOGY
Gothenburg, Sweden, 2020
CTH-NT-342/RR-23 June 2020

CTH-NT-342/RR-23 June 2020

Ringhals Diagnostics and Monitoring, Annual Research Report 2019-2020

I. Pázsit, L. A. Torres, C. Montalvo, L. Nagy, G. Klujber,
M. Szieberth, T. Misawa, Y. Kitamura, and H. Nylén

Nuclear Engineering Group
Division of Subatomic, High Energy and Plasma Physics
Chalmers University of Technology
SE-412 96 Göteborg, Sweden
ISSN 0281-9775

Ringhals Diagnostics and Monitoring, Annual Research Report 2019-2020

I. Pázsit, L. A. Torres, C. Montalvo, L. Nagy, G. Klujber,
M. Szieberth, T. Misawa, Y. Kitamura, and H. Nylén

Nuclear Engineering Group
Division of Subatomic, High Energy and Plasma Physics
Chalmers University of Technology
SE-412 96 Göteborg, Sweden

Abstract

This report gives an account of the work performed by the Division of Subatomic, High Energy and Plasma Physics (formerly, Division of Nuclear Engineering), Chalmers, in the frame of a research collaboration with Ringhals, Vattenfall AB, contract No. 686103-003. The contract constitutes a 1-year co-operative research work concerning diagnostics and monitoring of the BWR and PWR units. The work in the contract has been performed between July 1st 2019, and June 30th, 2020. Originally, we planned to work with five items as follows:

1. Continued investigation of possible baffle jetting in R3 with noise analysis of in-core and ex-core detector signals;
2. Further analysis of the vibrations of thimble tubes with axially dependent in-core measurements in various radial positions;
3. Evaluation of new ex-core measurements for beam mode and tilting mode vibrations in R3;
4. Experimental work and simulations in support of the use of fission chambers in the current mode for reactor diagnostics, as an alternative of pulse counting methods;
5. Development of a new method to determine the axial velocity profile of the void in the core of a BWR by using four permanent in-core LPRMs and a TIP detector.

Due to changed circumstances, mostly related to the Covid-19 pandemics, some changes were made in the project. Item #1 was reduced, whereas the work planned in item #2 was postponed to the next Stage. The work was performed by Imre Pázsit (project co-ordinator), Luis Alejandro Torres and Cristina Montalvo (research collaborators from UPM, Madrid), Lajos Nagy (double degree PhD student jointly with BME Budapest), Gergely Klujber and Máté Szieberth (research collaborators from BME), Tsuyoshi Misawa and Yasunori Kitamura (research collaborators from KURNS, Kyoto, Japan) and Henrik Nylén, the contact person at Ringhals.

CONTENTS

1. INTRODUCTION

This report gives an account of the work performed by the Nuclear Engineering Group of the Division of Subatomic, High Energy and Plasma Physics (former Division of Nuclear Engineering), Chalmers, in the frame of a research collaboration with Ringhals, Vattenfall AB, contract No. 686103-003. The contract constitutes a 1-year co-operative research work concerning diagnostics and monitoring of the BWR and PWR units. The work in the contract has been performed between July 1st 2019, and June 30th, 20209. Originally, we planned to work with six main items as follows:

1. Continued investigation of possible baffle jetting in R3 with noise analysis of in-core and ex-core detector signals;

2. Further analysis of the vibrations of thimble tubes with axially dependent in-core measurements in various radial positions;

3. Evaluation of new ex-core measurements for beam mode and tilting mode vibrations in R3;

4. Experimental work and simulations in support of the use of fission chambers in the current mode for reactor diagnostics, as an alternative of pulse counting methods;

5. Development of a new method to determine the axial velocity profile of the void in the core of a BWR by using four permanent in-core LPRMs and a TIP detector.

However, mostly due to the situation with the Covid-19 pandemics, some items had to be reduced or postponed. Items #1 and #2 required dedicated measurements, which could not be performed within the project period. Moreover, it turned out that the problem with baffle jetting (item #1) is not interesting in the continuation; partly, there is no indication of any damage, and partly, construction changes were made in Ringhals-3 which diminish possibility of the occurence of the problem. Hence only a simple analysis of the baffle jetting was made. The problem with thimble tube vibrations (item #2) is still interesting, but the evaluation of the delayed dedicaded measurements will be included into the next Stage of the project.

The present work was performed by Imre Pázsit (project co-ordinator in Chalmers), Luis Alejandro Torres and Cristina Montalvo (research collaborators from UPM, Madrid), Lajos Nagy (double degree PhD student jointly with BME Budapest), Gergely Klujber and Máté Szieberth (research collaborators from BME), Tsuyoshi Misawa and Yasunori Kitamura (research collaborators from KURNS, Kyoto, Japan) and Henrik Nylén, the contact person at Ringhals.

2. CONTINUED INVESTIGATION OF POSSIBLE BAFFLE JETTING IN R3 WITH NOISE ANALYSIS OF EX-CORE DETECTOR SIGNALS

The background of the origin of this subject was that a so-called upflow conversion is planned for the 2020 outage on R3, in order to minimise the risk for fuel damage from baffle jetting. At present the coolant flow outside the baffle plates is oriented downwards in R3, whereas it is upwards in R2 and R4. The general problem is the pressure difference between the outer side of the baffle plates and the core, in particular at the higher axial elevations. The bolts fixing the baffle structure are exposed to wear during longer times (due to thermal fatigue and fast neutron irradiation), which process can degrade the bolts, such that a gap can open at the inside corners of the baffle. Due to the pressure difference, jet streams can arise towards the interior of the core, which can lead to very strong vibrations of the individual fuel pins or the assemblies. Such a phenomenon can appear quite suddenly during the cycle. If it goes undetected, it can lead to serious damage of the fuel pins, including breakdown of the cladding.

No dedicated in-core measurements were performed in the current Stage to this end. In addition, the interest in this subject has been reduced, partly because there have not been any indications of damage that could be attributed to baffle jetting, and partly because as from the next cycle, R3 will operate with the upflow conversion completed, which further decreases the chances for damage. For all these reasons, it was decided that in this report, that a reduced analysis will be performed, in that only the latest ex-core measurements (i.e. those taken in this Stage) will be analysed, and this subject will not be pursued in the continuation.

The analysis goes on the same lines as in the previous Stage. As it was noted, from the point of view of ex-core neutron noise, baffle jetting can possibly be identified from the deformations it incurs in the core-barrel structure, and therefore its effect on the ex-core neutron noise. From the mechanical nature of the problem, baffle jetting is expected to lead to shell-type vibration modes, but also to a uniform radial increase of the core size, i.e. core widening (zeroth azimuthal mode). Such a phenomenon is known from the Phenix Sodium Fast Reactor measurements [1]; and it was termed “core flowering”. From the symmetry properties of the core widening, it is clear that its presence in the detector signals can be enhanced with the addition of all four detector signals at the same axial level, which is the same as the enhancement of the reactivity term. However, the frequency of the core widening effect is expected to be different from that of the reactivity effect, induced by the individual vibrations of the fuel assemblies at 8 Hz; rather, it should lie closer to the shell mode vibrations.

In addition, due to the thermal hydraulics conditions, such deformations are expected to lead to larger changes at the upper part of the core than at the lower part). Hence the effect of baffle jetting would be consistent with the amplitude of

the peak corresponding to the core widening effect, as well as to that of the shell mode, was larger in the upper detectors than in the lower detectors.

To this end, the shell mode components and the reactivity components were compared between the upper and lower detectors for all three measurements. Figs. 2.1, 2.2 and 2.3 show the shell mode components for the three measurements. The shell mode is represented by the peak at 20 Hz. It is seen that in all three measurements the peak at 20 Hz is larger for the upper detectors than for the lower detectors. This is in clear contrast to the amplitudes of the beam-mode vibrations around 8 Hz, where, for obvious reasons, the amplitudes of the peaks are larger in the lower detectors than in the upper ones. The reversed relationship for the shell mode vibrations could be an implicit indication of baffle jetting. These findings are in complete agreement with those of the previous Stage, hence no change in the status of the core can be observed in this respect.

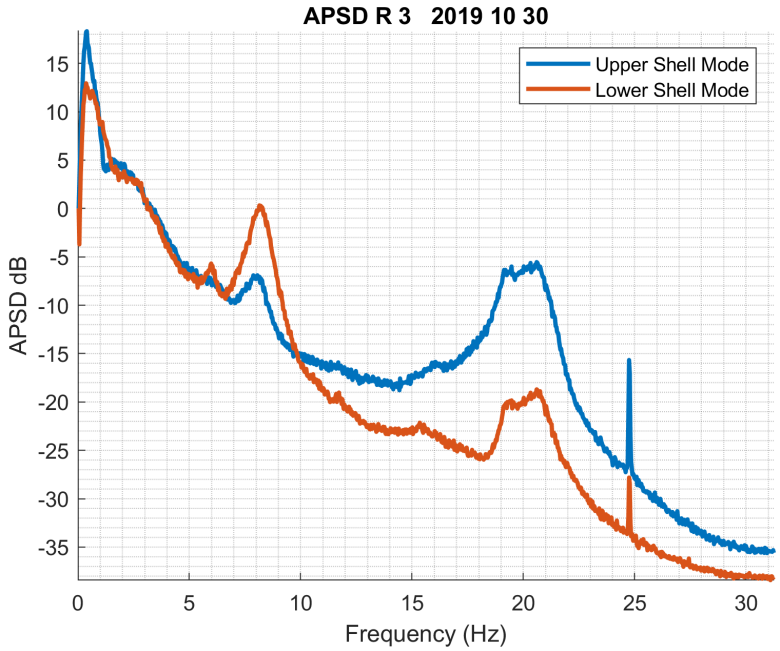

Figure 2.1: APSDs of the shell mode in Measurement 1

Figs 2.4, 2.5 and 2.6 show the comparison for the reactivity component between the upper and lower detector for the three measurements. Again, these results are in complete agreement with those of the previous Stage. It is seen that, in addition to the peak at 8 Hz, there is also a peak at around 15.5 - 15.6 Hz. In agreement with the discussions in the previous Stage and also those above, it is conceivable that this peak corresponds to the core widening. This assumption is corroborated by the fact that the amplitude of the peaks in all three measurements is higher in the upper detectors than in the lower detectors. This amplifies the assumption that this peak is related to the core widening effect, and it is in agreement with the observations for the shell mode vibrations.

In summary, by identifying the reactivity-like component at 15.5 Hz as the core widening component, it is found that both the shell mode component, as well as the

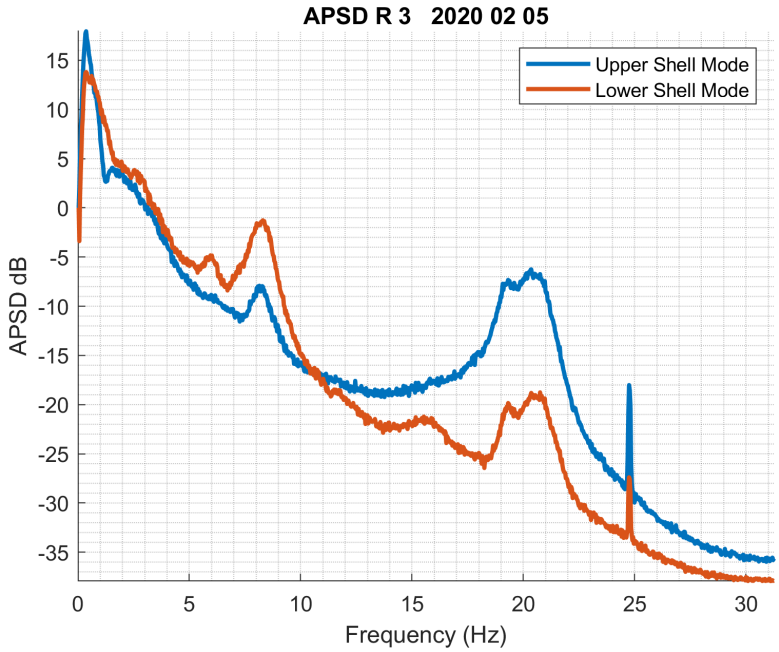

Figure 2.2: APSDs of the shell mode in Measurement 2

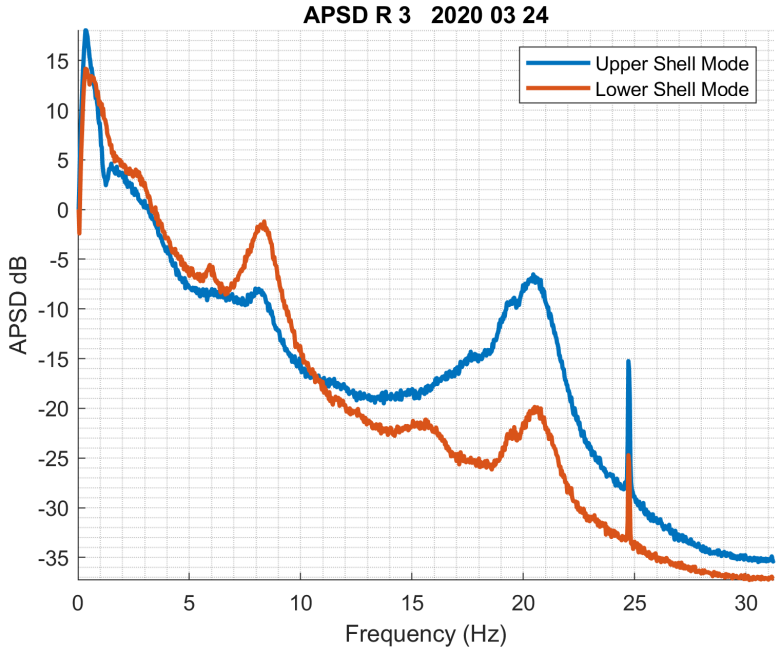

Figure 2.3: APSDs of the shell mode in Measurement 3

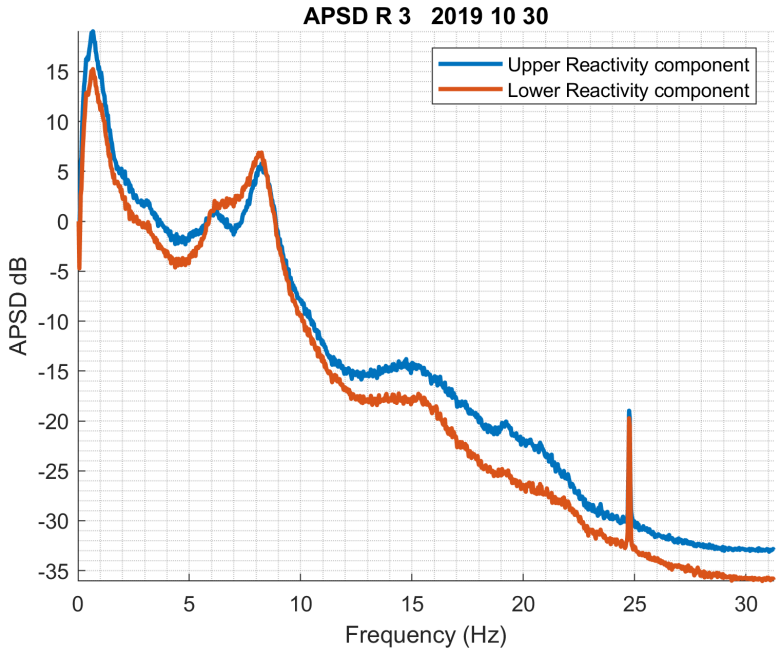

Figure 2.4: APSDs of the reactivity component in Measurement 1

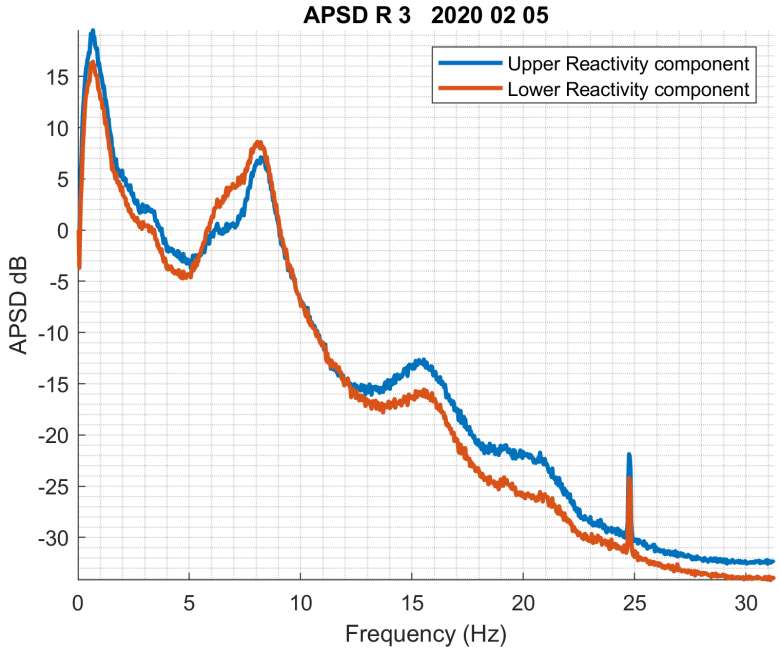

Figure 2.5: APSDs of the reactivity componen in Measurement 2

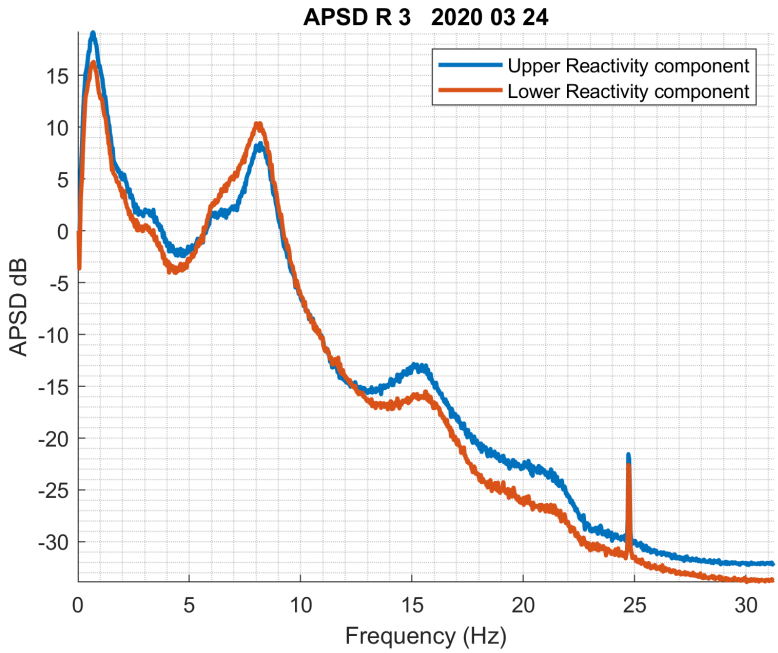

Figure 2.6: APSDs of the reactivity component in Measurement 3

core widening component, exhibit a larger amplitude peak for the upper detectors than for the lower detectors. This might indicate the presence of baffle jetting. However, because of the sparse azimuthal placing of the ex-core detectors, as well as the global character of the ex-core signals, it is not possible to identify the position(s) of possible baffle jetting with a resolution with respect to the azimuthal position. Moreover, the statement on the possible presence of baffle jetting is based only on a qualitative comparison of the peaks, and similarly to the case of beam mode vibrations, it does not give an indication of the amplitude of the corresponding vibrations, and hence also it cannot be used for the indication of the severity of the vibrations. However, no indications of baffle jetting, such as wear marks on fuel rods at spacer grid positions, could be identified during aimed inspections of fuel assemblies at Ringhals 3 during the outages in 2018, 2019 and 2020. Together with the upflow conversion performed during the refuelling during 2020, i.e. about the end of the present Stage, it was decided that this subject will not be investigated in the continuation of the project.

3. FURTHER ANALYSIS OF THE VIBRATIONS OF THIMBLE TUBES WITH AXIALLY DEPENDENT IN-CORE MEASUREMENTS IN VARIOUS RADIAL POSITIONS

The measurements were not performed during this project period, but they are planned for the beginning of the next cycle. They will be evaluated and reported in the next Stage.

4. EVALUATION OF NEW EX-CORE MEASUREMENTS FOR BEAM MODE AND TILTING MODE VIBRATIONS IN R3

4.1 Introduction and background

The analysis of core-barrel vibration properties (often abbreviated to CBM, core barrel motion) have been the subject of study both in Sweden and internationally. It has also been the subject of the collaboration between Chalmers and Ringhals from the beginning, as it was reported in several previous Stages in the Ringhals diagnostic project [2, 3, 4, 5, 6, 7, 8, 9, 10, 11, 12, 13].

Within the last decade, a series of studies dedicated to core barrel vibrations have been performed in order to analyse and find a suitable explanation for the recent observations of wear at both the lower and upper core-barrel-support structures, i.e. the lower radial key and the reactor vessel alignment pins in the Ringhals PWRs. In the last few years the main focus in this area was put on the investigation of a double peak observed in the Auto Power Spectrum in the frequency region of the beam mode component, mostly in measurements made in R4. A hypothesis was formulated about the nature of this peak, where it was suggested that the lower frequency peak is due to the beam mode vibrations and the upper peak is due to fuel assembly vibrations. A test of this hypothesis was one of the main targets of the analysis. A key factor of the analysis was to assume that the lower frequency peak is due to the (coherent) vibrations of the whole core barrel, hence the symmetries between the ex-core detectors could be used to enhance the effect, as well as to condense the quantification to one single parameter by taking combinations of the detector signals. However, the higher frequency mode was assumed to be due to the effect of the independent (incoherent) vibrations of the individual fuel assemblies, hence no symmetries could be utilised, and the results could not be condensed into one single parameter.

In 2014 a further, new assumption was made, in that the main effect of the individual vibrations manifests itself through the combined reactivity effect of all the individually vibrating fuel assemblies. This assumption, through the associated symmetries of the reactivity component, allowed to condense the analysis of the different detector signals into one single parameter even for the higher frequency peak. This hypothesis was tested with a fruitful outcome on the measurements taken at Ringhals-4. In addition, although no double peak was visible in the APSDs of the R3 measurements, with the peak separation and curve fitting technique, the two peaks could be separated even in the R3 measurements. Thus, finally, it became possible to distinguish between the beam mode component due to core barrel vibrations and the reactivity component associated to the single fuel assembly vibrations. In addition, through numerical simulations, it was also possible to confirm the constant amplitude within one fuel cycle for the beam mode component, and the varying amplitude (within one cycle) of the reactivity component (individual fuel assembly vibrations), which were in good agreement with the original hypothesis.

The work in the continuation was therefore not concentrated any longer to the test and proof of the hypothesis, and the associated trend analysis of the evolution of the peak amplitudes during the cycle, rather on checking whether there is any major change in the amplitude and frequency of the beam mode peaks, as compared to the previous measurements, which could indicate an increased play in the lower radial key support. A special circumstance in this aspect is that in 2015, the total power of Ringhals-4 was increased by 18.6 %. Another aspect is that some structural changes took place in R4. The hold-down springs were replaced during the outage in 2013, and the interior parts were lifted out during the outage in 2014 for an inspection. As it was seen and reported in the previous Stages [12, 13], this has changed the shape of the spectra around the beam mode frequency such that the visibility of the former double peak has ceased and only one peak could be observed visually. As the results of the previous Stage showed, by this change, the ex-core neutron spectra became very similar between R3 and R4.

Lastly, as it was described in the previous Stages [11, 12, 13], a new type of pivotal vibration mode, which we named as "tilting" or "wobbling" mode, was discovered. The separation of the tilting mode from the other components is made with methods similar to the other mode separation methods with adding and subtracting the signals in various combinations. The only difference is that for the separation of the tilting mode from the other components, all 8 detectors (the four ex-core detectors at two axial elevations) need to be used. Hence in the routine analysis, the separation of all four components (beam, shell, reactivity and tilting modes) has been made in the continuation.

In the previous Stage (2018-19), the ex-core measurements were made in R3. Since in the years preceding Stage 2018, the ex-core measurements were performed in R4, there was no immediate possibility to compare the new measurements with R3 to immediated previous ones. One could note that unlike in the previous R4 measurements, the double peak at 8 Hz could not be seen in the spectra, they could only be separated by a refined curve fitting procedure. The trend analysis showed that the two modes around 8 Hz behaved practically the same way within the cycle, which was another difference compared to the previous R4 measurements. In the present Stage, the ex-core measurements were made again in R3, which gives a possibility to compare the present measurements with those of the previous Stage.

4.2 Details of the measurements in R3

Three sets of measurements were analysed. The measurements were performed in R3 in cycle 37, on 30 October 2019, as well as 5 February and 24 March 2020. For simplicity they will be referred to as Measurement 1, 2 and 3 respectively. The sampling frequency was 62.5 Hz for all three sets of measurements. The measurement points are shown in Table 4.1. More detailed data regarding settings and general parameters can be found in the measurement protocols from previous measurements, which were performed in an identical manner [14, 15, 16].

Table 4.1: The measurement data structure of the three measurements in Ringhals 3 during 2019-20.

Channel	**Measurement point**
0	Time
1	N41U DC
2	N42U DC
3	N43U DC
4	N44U DC
5	N41L DC
6	N42L DC
7	N43L DC
8	N44L DC
9	N41U AC
10	N42U AC
11	N43U AC
12	N44U AC
13	N41L AC
14	N42L AC
15	N43L AC
16	N44L AC

4.3 Analysis of the measurements made on 2019-10-30 (Measurement 1)

4.3.1 Individual spectra of all detectors

In a general summary, it can be stated that the results of the evaluation of the measurements in the present Stage are thoroughly similar to those in the previous Stage. There are certain smaller deviations, but they do not bear any significance. Some slight differences will be noticed in the trend analysis, but this is more due to a refinement in the mode separation technique than the changing of the status of the plant. Actually, the trend analysis was repeated for the measurements of the previous Stage with the refined method, and then the present and the previous Stage showed very similar results.

The APSDs of all eight individual detector signals are shown in Fig. 4.1. They are very similar to those from the previous Stage. All signals show the two familiar peaks around 8 and 20 Hz for the beam and shell modes, respectively. Similarly to the previous measurements made in R3, as well as in the latest measurements in R4, no double peak is visible at 8 Hz. Rather, similarly to the previous measurements, a small peak is visible around 6 Hz in most, but not all detector spectra, i.e. it is much more separated from the 8 Hz peak in frequency. On the other hand, the two peaks that can be identified with the beam mode and the reactivity mode (corresponding to the noise induced by the individual fuel assembly vibrations) cannot be visibly separated. This will be reflected in the detailed analysis below. A general observation is that after the replacement of the hold-down springs in R4 during the outage in 2013, and lifting out the interior parts during the outage in 2014 for an inspection, the ex-core detector spectra in R4 and R3 look now rather similar.

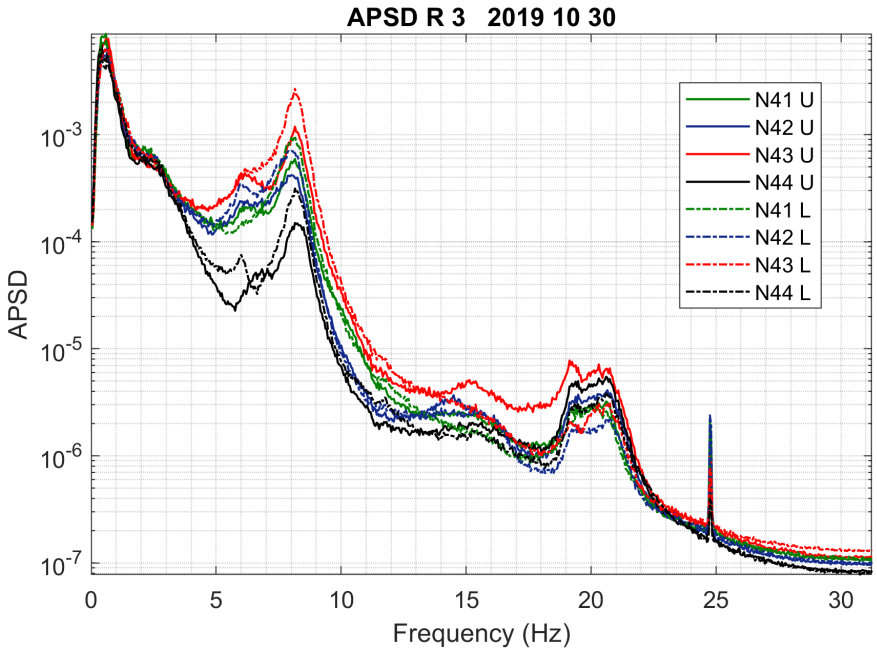

Figure 4.1: APSDs of all 8 ex-core detector signals from Measurement 1

.

4.3.2 Results of the mode separation

The beam mode, shell mode, reactivity component and the tilting modes were separated according to the detector signal combination principles as in the previous work. The results are shown for the upper detectors in Fig. 4.2, and for the lower detectors in Fig. 4.3. The result of the separation is rather similar for the two cases, as well as to those of the previous Stage. It is seen that the amplitude of the beam mode is larger for the lower detectors, as expected, whereas the amplitude of the other components is very similar for the upper and lower detectors.

One peculiar fact, observed already in the previous Stage, is that the shell mode, which shows only a small peak at 8 Hz in the upper detectors signals (which is expected) has a quite distinct peak at 8 Hz in the lower detector signals (not expected). This is somewhat surprising, and there is no direct explanation of it. This phenomenon did not appear in the previous R4 measurements, although in some of the spectra the shell component shows a small, but noticeable peak around 8 Hz [12].

Similarly to the results of Stage 2016 [12] reporting on measurements made in R4, as well as Stage 2018 (R3) [13], one notes a small peak around 15.5 Hz in both the upper and the lower detector signals in the reactivity component. In Stage 2016 our interpretation was that since this frequency is about twice that of the pendular fuel vibration frequency at 8 Hz, which is also identified as a reactivity effect, the peak at 16 Hz can be attributed to the higher harmonics of the fuel assembly vibrations at the fundamental frequency 8 Hz. However, based on the analysis of the baffle jet effect in Stage 2018, it is more likely that this peak is due to the "core flowering" effect, i.e. the zeroth azimuthal mode of the core barrel.

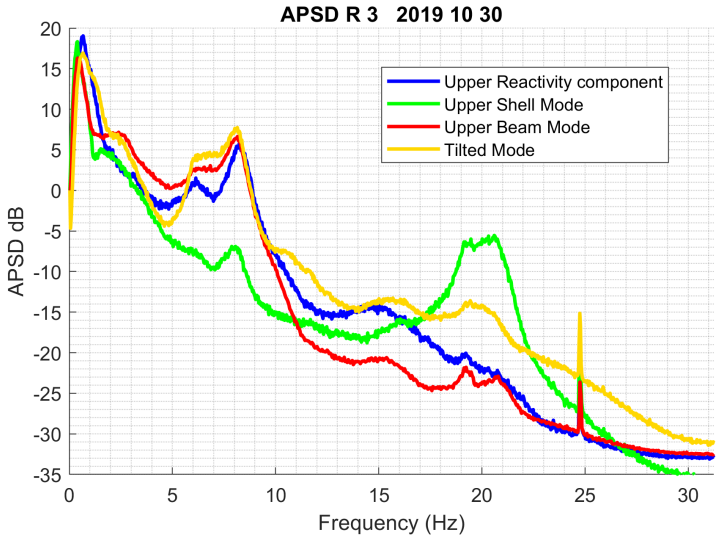

Figure 4.2: APSDs of the beam mode, shell mode, reactivity component and the tilting mode for the upper detectors, extracted from Measurement 1.

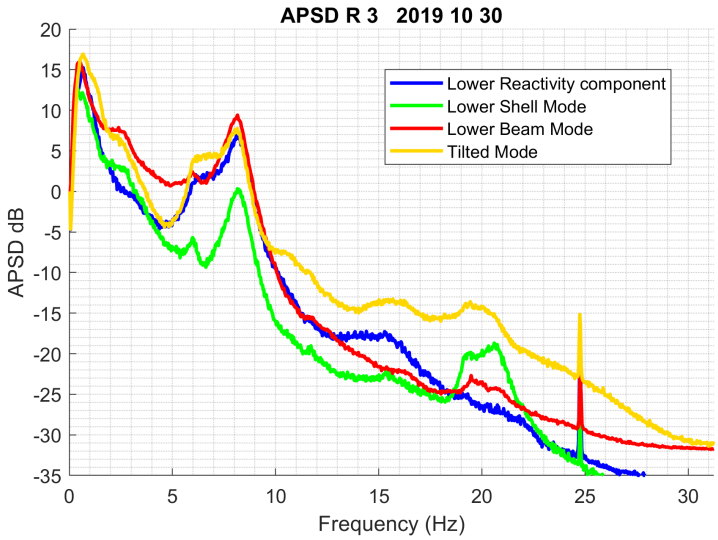

Figure 4.3: APSDs of the beam mode, shell mode, reactivity component and the tilting mode for the lower detectors, extracted from Measurement 1

4.3.3 Phase and coherence relationships between the upper and lower detectors

An analysis of the coherence and the phase relationships between detectors at the same and different axial levels was performed, similarly to that in the previous stages. The coherence and phase between the diagonally opposite detectors N41 and N42, for both the same and different axial levels, is shown in Fig. 4.4, and the same for detectors N43 and N44 in Fig. 4.5. The coherence and phase between the upper and lower detectors at the same radial position, for all four detectors, is shown in Fig. 4.6.

Again, these results are very similar to those of the previous Stage. As already mentioned in the previous Stage, for the detector pair N41 - N42, Fig. 4.4, the coherence differs from the previous R4 patterns. Unlike in the R4 measurements, the coherence around 8 Hz is very low, which is surprising, given the fact that the APSD peaks are the highest in this fequency region, and the phase is rather solidly 180°, without much scatter, up to about 8 Hz, where it shifts to zero. The coherence has though a medium large peak at around 4 Hz, which is somewhat more resembling to the former measuremens in R4.

One possible explanation of the low coherence at 8 Hz could be if the beam mode vibrations are highly anisotropic, and are perpendicular to the line connecting the detectors N41 - N42. Another possibility is an interference between the beam mode, the reactivity mode and the tilting mode. As it is seen in Figs 4.2 and 4.3, all these components have comparable amplitudes at 8 Hz, but they are not correlated to each other.

The phase behaviour is in line with the previous R4 measurements, and also with the expectation that just below 8 Hz the beam mode vibrations dominate, which is the cause of the out-of-phase behaviour, after which, at a slightly higher frequency,

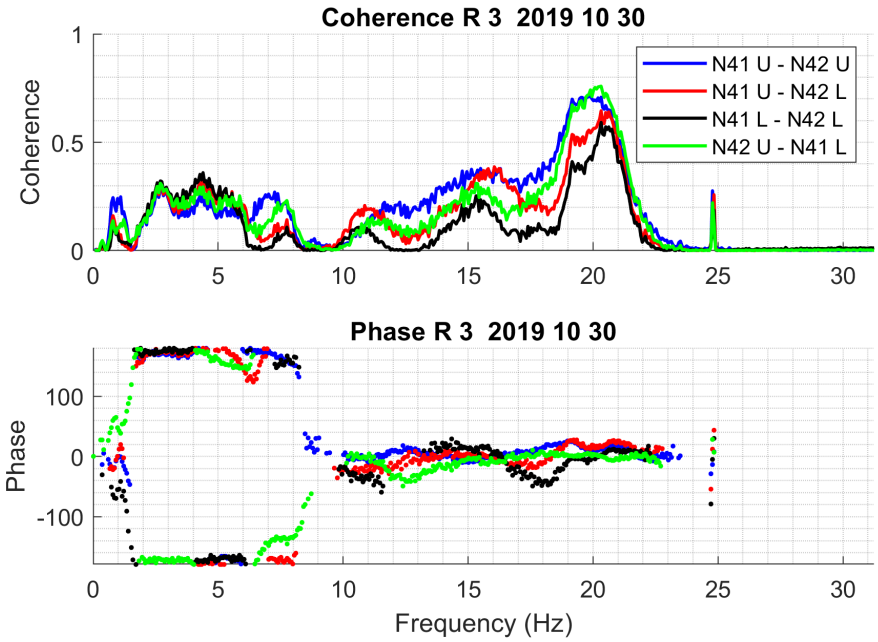

Figure 4.4: The coherence and the phase of the CPSD calculated for the N41U-N42U, N41U-N42L, N41L-N42L and N42U-N41L detector pairs in Measurement 1.

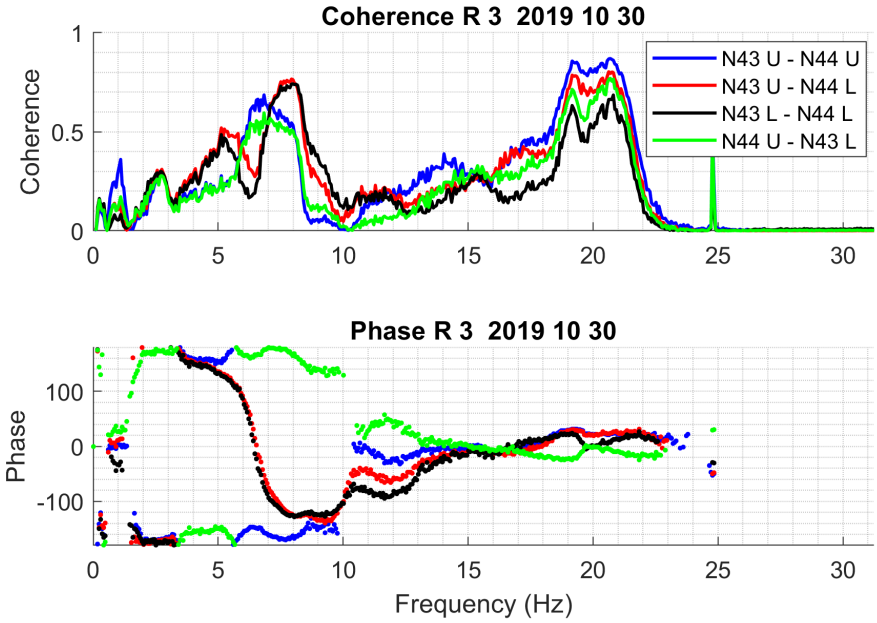

Figure 4.5: The coherence and the phase of the CPSD calculated for the N43U-N44U, N43U-N44L, N43L-N44L and N44U-N43L detector pairs in Measurement 1.

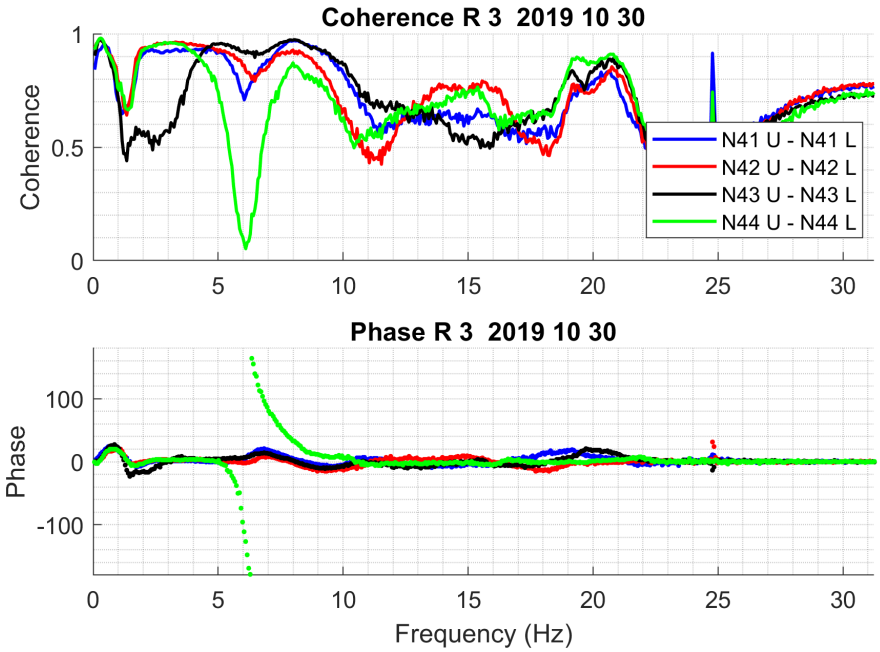

Figure 4.6: The coherence and the phase of the CPSD calculated for the N41U-N41L, N42U-N42L, N43U-N43L and N44U-N44L detector pairs in Measurement 1.

the reactivity effect of the fuel assembly vibrations take over, which is the cause of the zero phase above 8 Hz.

The picture is rather different for the detector pairs N43 - N44, Fig. 4.5. Like in the previous Stage, and also similarly to the former R4 measurement, the coherence is much larger at 8 Hz, as expected. Actually, now the coherence is high for all four pair combinations, whereas in the previous stage, it was only high for two of the four possible detector combinations. The phase behaviour also deviates somewhat from that in the previous Stage, in that for the combinations N43U-N44U and N44U-N43L, it shows the same out-of-phase behaviour as for the detectors N41 and N42, whereas the other two pairs show the same behaviour as in the previous Stage, i.e. it changes continuously from 180° to -180°. One can say that the coherences and phases between the detectors N43-N44 now resemble more to the expected behaviour than in the previous Stage.

As discussed in the previous report, the type shifting (not constant) phase behaviour is unknown from previous measurements, and it is rather difficult to interpret in the context of core barrel vibrations. A linear phase between two detectors is an indicator of a (deterministic) time delay between the two signals, which is hardly conceivable for the ex-core detector signals induced by vibrations. One cannot exclude though the possibility that the vibrations are periodic and not random, in which case the conclusions drawn from the coherence and phase are not valid, since these are only defined for random processes. However, the large qualitative difference between the phase and coherence between the pairs N41 - N42 on the one hand and N43 - N44 on the other, supports the assumption that the CBM may be highly anisotropic.

Regarding the axial coherence and phase between detectors at the same radial position, Fig. 4.6, these are very similar to those of the previous Stage. There is a quite deep dip in the coherence and a deviation from zero phase at 6 Hz only for the detectors N44 upper and lower. All other three radial pairs have high coherence and zero phase throughout this region. Similar deviation between one detector and the other three has also been observed in other measurements, both in R3 and R4.

4.4 Analysis of the measurements made on 2020-02-05 (Measurement 2)

4.4.1 Individual spectra of all detectors

The APSDs of all eight individual detector signals are shown in Fig. 4.7. These look very similar to those in Measurement 1. A moderate increase of the amplitude of the 8Hz peak is seen. No noticeable deviation from the results of the previous Stage can be seen.

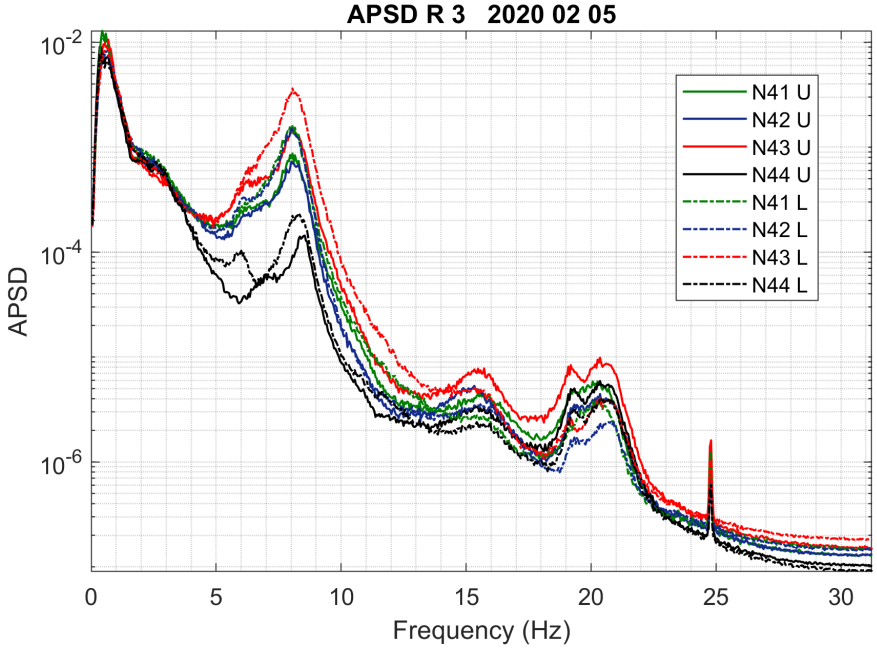

Figure 4.7: APSDs of all 8 ex-core detector signals from Measurement 2

.

4.4.2 Results of the mode separation

The results for the separation of the beam mode, shell mode, reactivity component and the tilting modes are shown for the upper detectors in Fig. 4.8, and for the lower detectors in Fig. 4.9. These results are very similar to those of Measurement 1. That is, the amplitude of the beam mode is larger for the lower detectors, and the frequency of the reactivity mode is somewhat higher than that of the beam mode, as expected. The amplitude of shell mode at 8 Hz has decreased somewhat in the lower detectors.

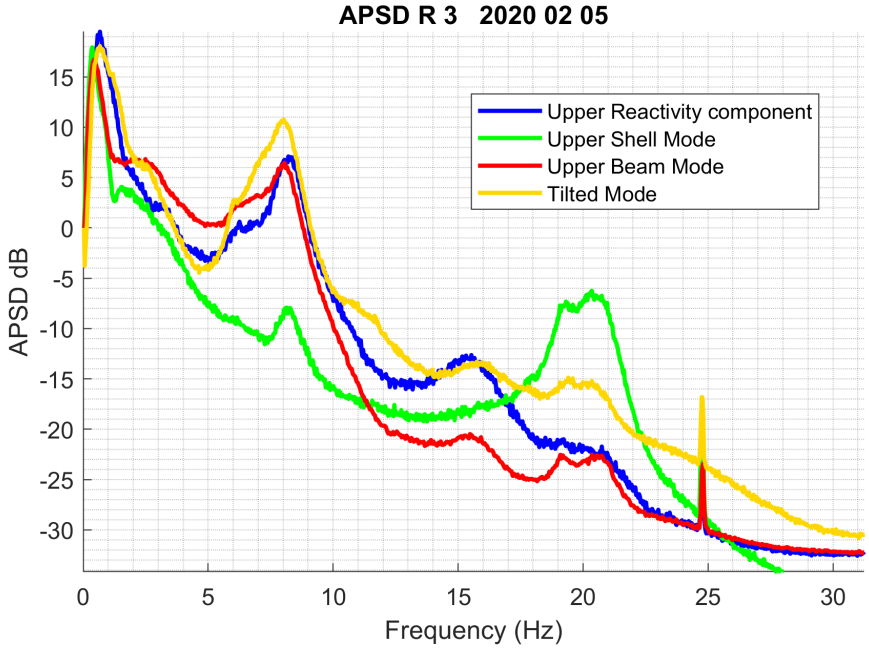

Figure 4.8: APSDs of the beam mode, shell mode, reactivity component and the tilting mode for the upper detectors, extracted from Measurement 2.

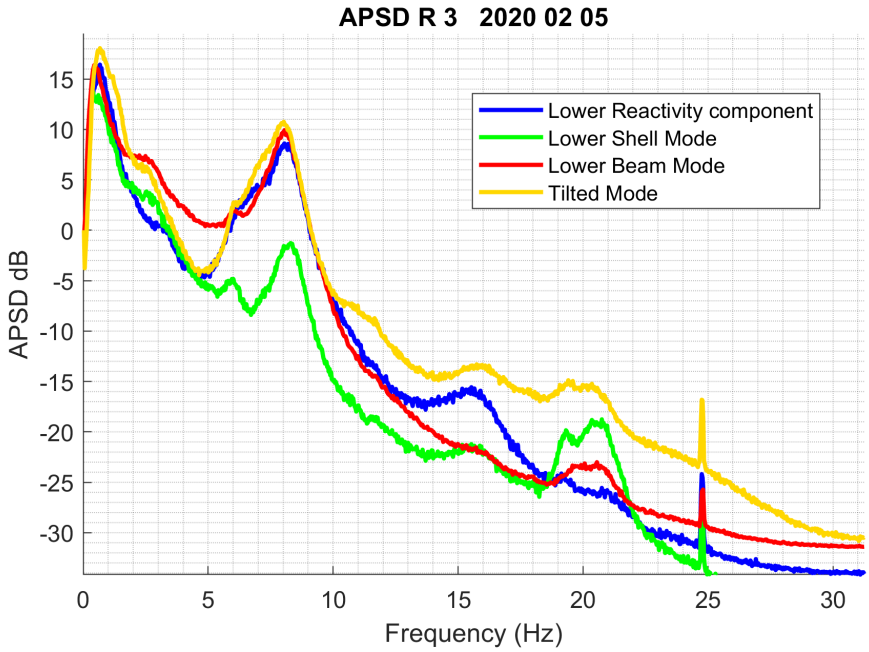

Figure 4.9: APSDs of the beam mode, shell mode, reactivity component and the tilting mode for the lower detectors, extracted from Measurement 2

4.4.3 Phase and coherence relationships between the upper and lower detectors

The coherences and phases between the diagonally opposite detectors N41 and N42, for both the same and different axial levels, are shown in Fig. 4.10, and the same for detectors N43 and N44 in Fig. 4.11. The coherences and phases between the upper and lower detectors at the same radial position, for all four detectors, is shown in Fig. 4.12.

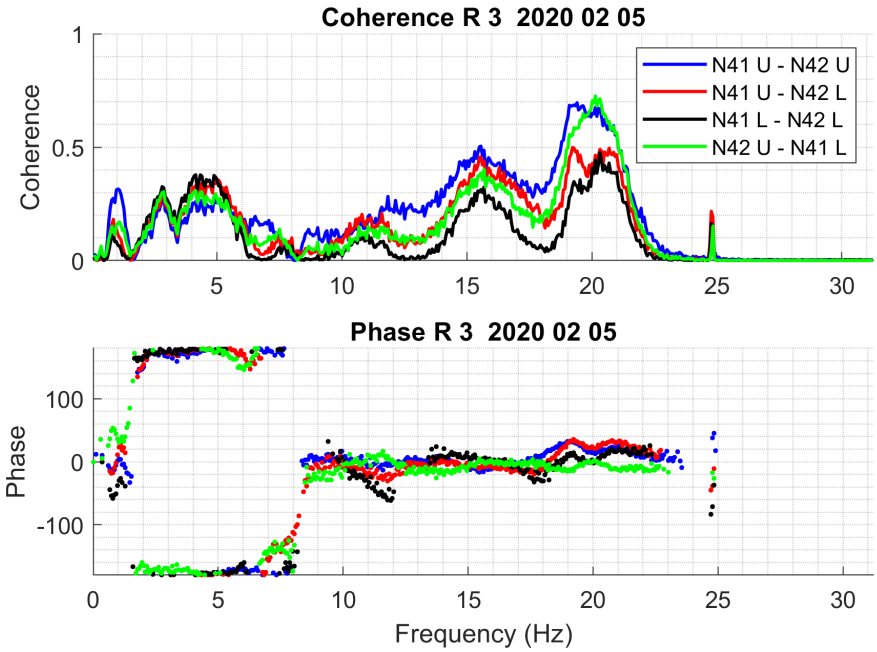

Figure 4.10: The coherence and the phase of the CPSD calculated for the N41U-N42U, N41U-N42L, N41L-N42L and N42U-N41L detector pairs in Measurement 2.

Similarly to the individual spectra and those from the results of the mode separation, these coherence and phase plots show a full resemblance to those in Measurement 1, and to the results of the previous Stage. In the phase of the axial detector pair N44U - N44L, which behaves differently from the other three pairs, the deviation of the phase from zero at around 6-7 Hz is larger than in measurement 1. Otherwise the interpretation and remarks remain the same as for measurement 1.

4.5 Analysis of the measurements made on 2020-03-24 (Measurement 3)

4.5.1 Individual spectra of all detectors

The APSDs of all eight individual detector signals are shown in Fig.4.13. These look again similar to those the previous two measurements. The amplitude of the peak at 6 Hz is still low.

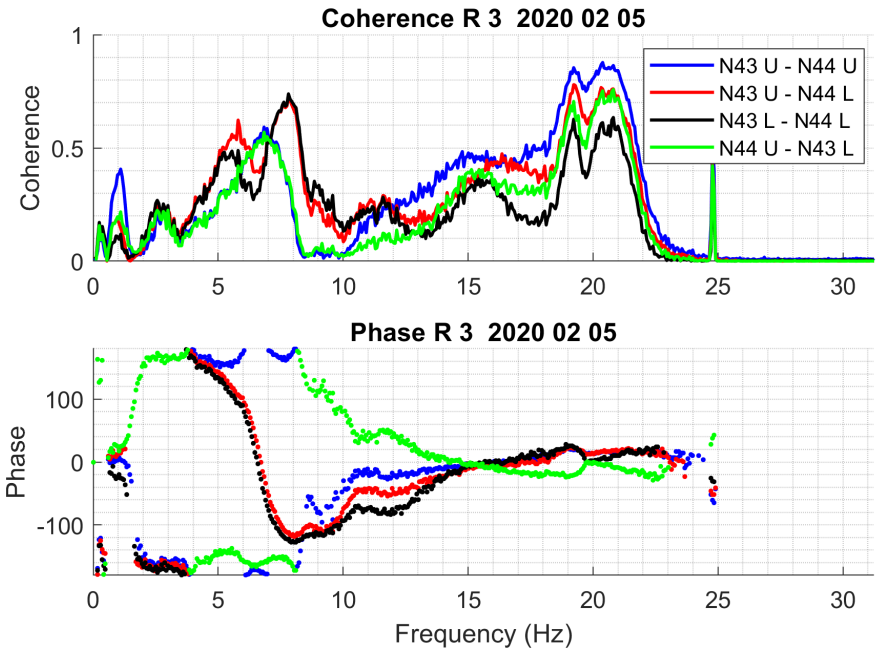

Figure 4.11: The coherence and the phase of the CPSD calculated for the N43U-N44U, N43U-N44L, N43L-N44L and N44U-N43L detector pairs in Measurement 2.

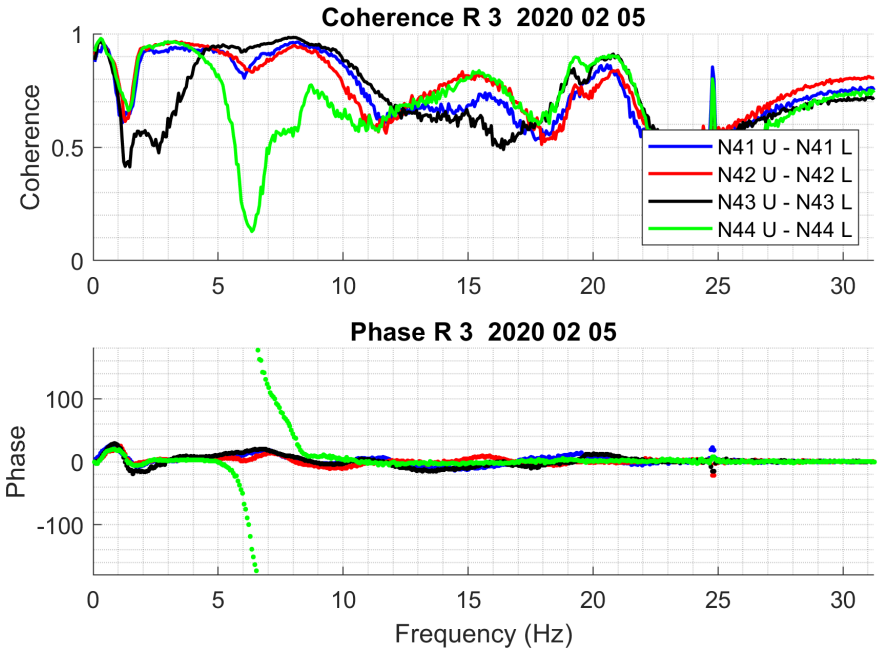

Figure 4.12: The coherence and the phase of the CPSD calculated for the N41U-N41L, N42U-N42L, N43U-N43L and N44U-N44L detector pairs in Measurement 2.

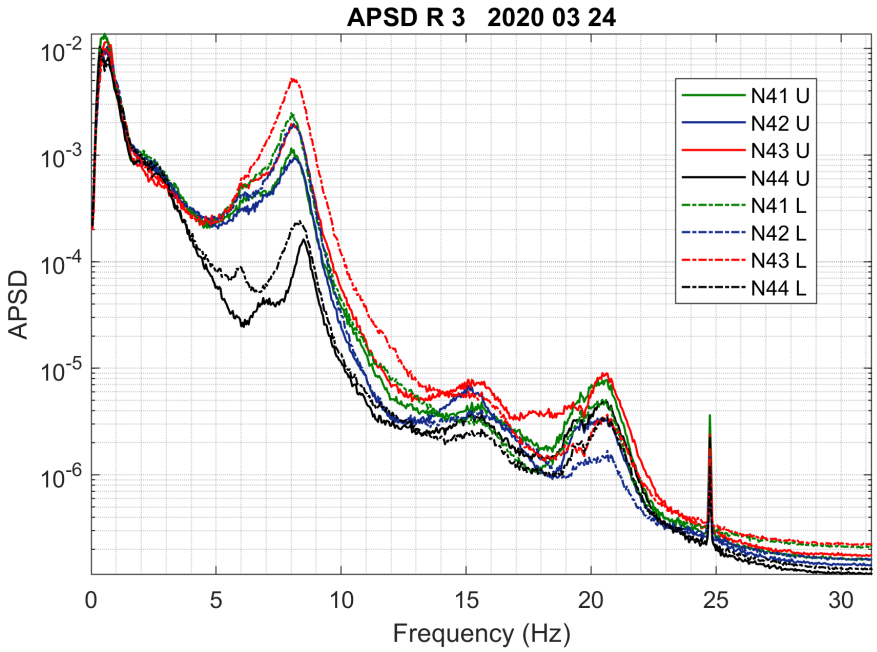

Figure 4.13: APSDs of all 8 ex-core detector sigals from Measurement 3

.

4.5.2 Results of the mode separation

The results for the separation of the beam mode, shell mode, reactivity component and the tilting modes are shown for the upper detectors in Fig. 4.14, and for the lower detectors in Fig. 4.15. The (unexpected) peak in the shell mode at 8 Hz is now diminished in the upper detector signals, whereas it remained still large in the lower detectors. The trend behaviour is somewhat opposite to that of the previous Stage, where the peak became stronger in the upper detectors towards the end of the cycle, whereas here it decreased.

4.5.3 Phase and coherence relationships between the upper and lower detectors

The coherence and phase between the diagonally opposite detectors N41 and N42, for both the same and different axial levels, is shown in Fig. 4.16, and the same for detectors N43 and N44 in Fig. 4.17. The coherence and phase between the upper and lower detectors at the same radial position, for all four detectors, is shown in Fig. 4.18.

Again, apart from some minor differences, the structure of all these plots is similar to the previous two measurements. The deviation of the phase from zero around 7 Hz between the detectors N44U - N44L is still pronounced, similarly to Measurement 2.

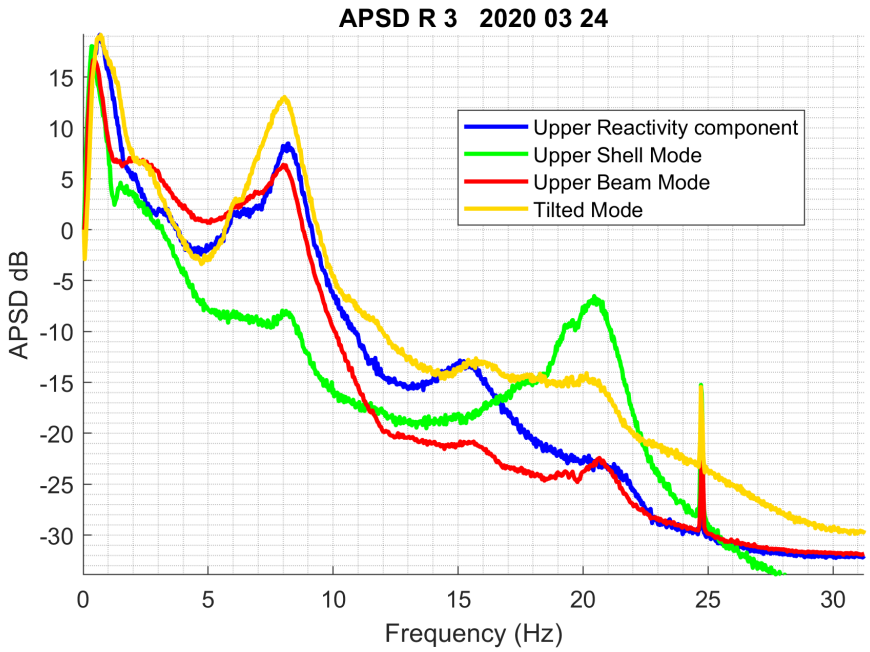

Figure 4.14: APSDs of the beam mode, shell mode, reactivity component and the tilting mode for the upper detectors, extracted from Measurement 3.

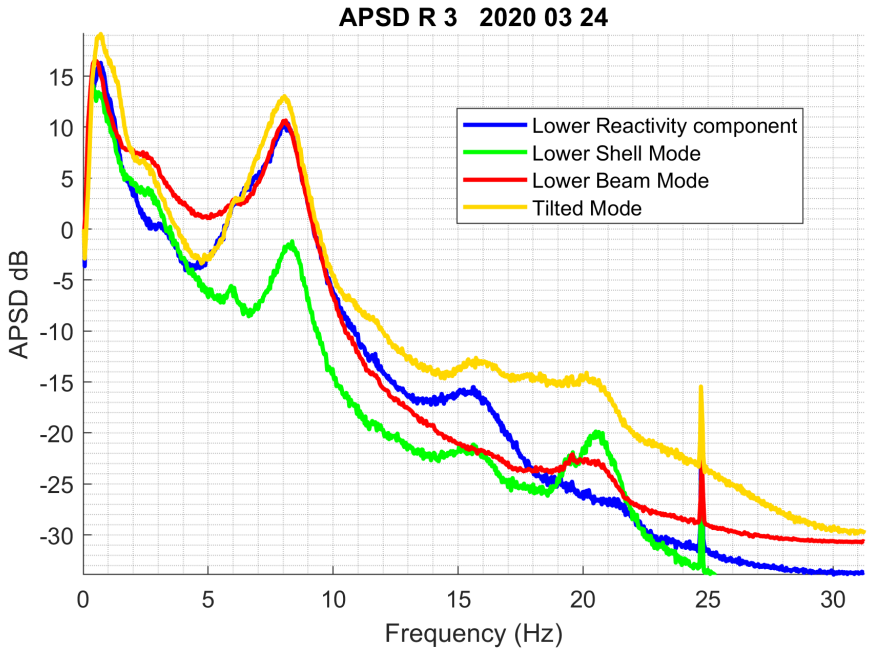

Figure 4.15: APSDs of the beam mode, shell mode, reactivity component and the tilting mode for the lower detectors, extracted from Measurement 3.

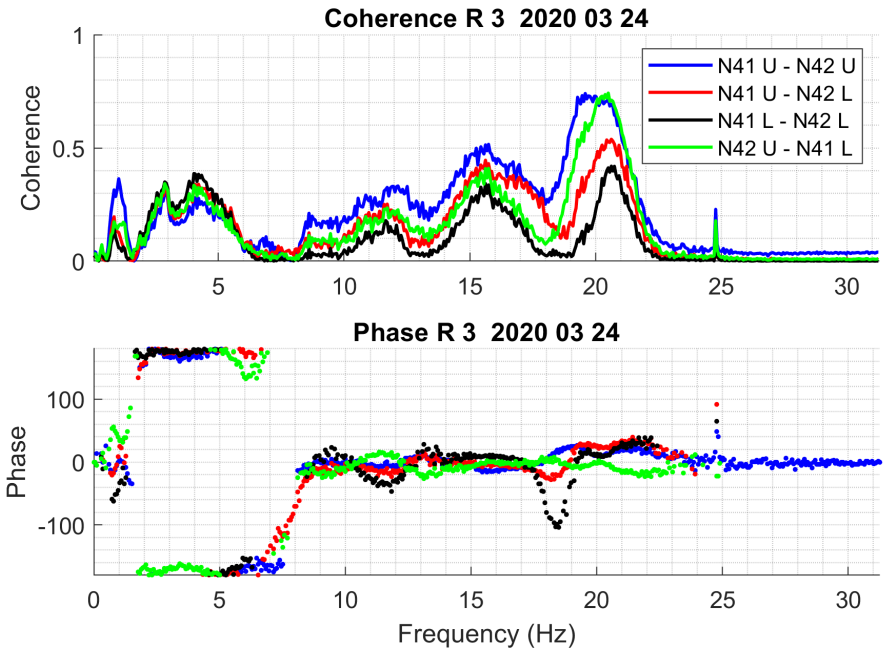

Figure 4.16: The coherence and the phase of the CPSD calculated for the N41U-N42U, N41U-N42L, N41L-N42L and N42U-N41L detector pairs in Measurement 3.

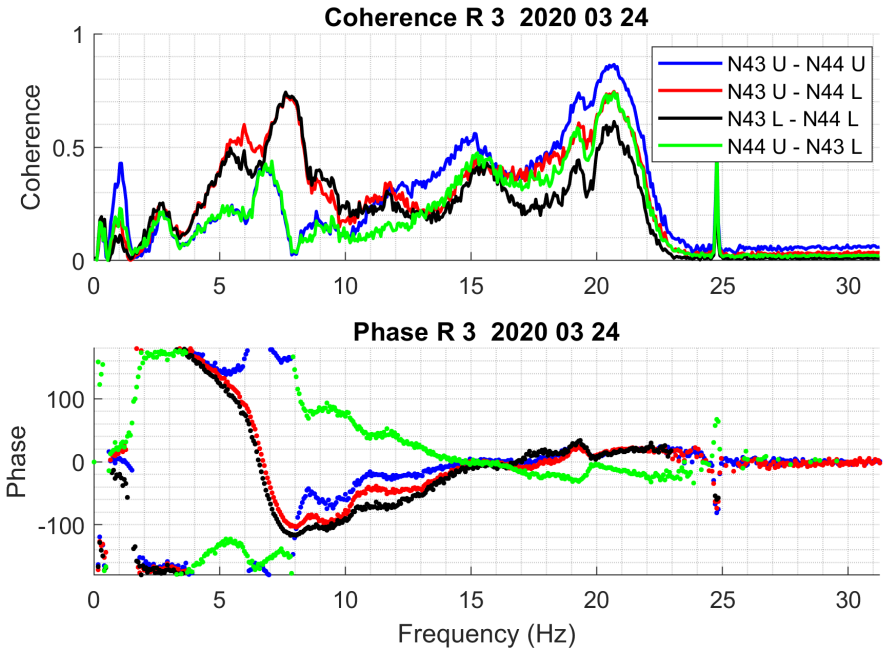

Figure 4.17: The coherence and the phase of the CPSD calculated for the N43U-N44U, N43U-N44L, N43L-N44L and N44U-N43L detector pairs in Measurement 3.

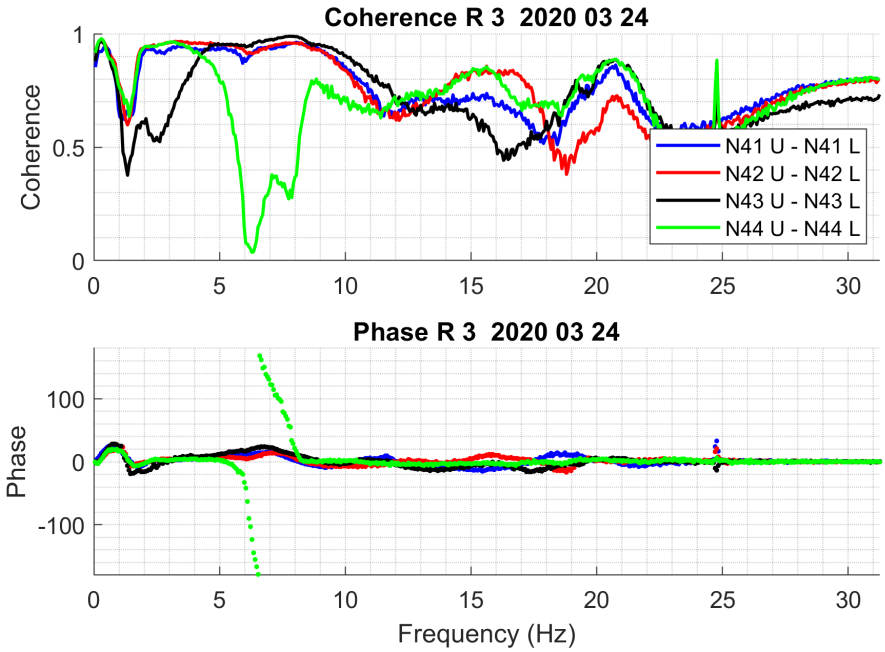

Figure 4.18: The coherence and the phase of the CPSD calculated for the N41U-N41L, N42U-N42L, N43U-N43L and N44U-N44L detector pairs in Measurement 3.

4.6 Trend analysis within the cycle

Whenever there are three measurements available in a cycle, a trend analysis, showing the development of the amplitudes of the beam and reactivity modes, also called Mode 1 and Mode 2, is of interest. This analysis has been relatively difficult in the last measurements both in R3 and R4, due to the difficulties in separating two peaks very close to each other in frequency. Therefore some further refinement of the curve fitting and mode separation method was made by our collaborators at UPM. The algorithm itself was not changed, but the way it is applied was improved based on the accummulated user experience. The fitted parameters are found in an iteration process, and the accuracy of the parameter fitting can be improved by refining the criteria for the termination of the iterations, which leads to performing more iterations. This improved iteration process was implemented in all analyses made this year, and it will be referred to as the "refined procedure".

The trend analysis this year was also made by the refined method. The results of the curve fitting are illustrated in Fig. 4.19 for both the upper and the lower detectors from Measurement 1 and Measurement 3.

The result of the trend analysis for both Modes is shown in Fig. 4.20. The evolution of the amplitudes is smoother than it was seen in the last Stage, where Mode 2 had a non-monotonic behaviour in the upper detectors. Now both the upper and the lower detectors give a monotonic increase for both Modes.

This means that the behaviour is similar between the present and the previous Stages, but it also deviates from the previous measurements in R4, where only one of the modes (Mode 2) did increase during the cycle. It also contradicts our previous

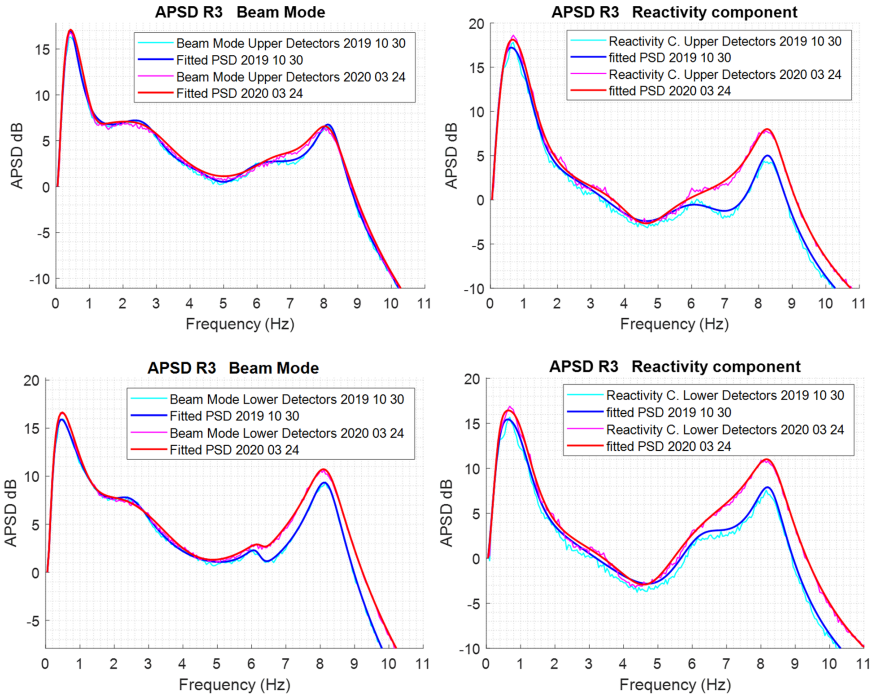

Figure 4.19: Results of the curve fitting for Measurements 1 and 3 to the peak around 8 Hz for the reactivity component (left side), and the beam mode (right side), both for the upper detectors (upper figures) and the lower detectors (lower figures).

hypothesis on the character and expected behaviour for the two Modes, according to which Mode 1 (the beam mode) is practically constant during the cycle and only Mode two (individual fuel vibrations) increase in amplitude. On the other hand, the results of this Stage are in a complete agreement with those of the previous one.

4.7 Long term trend analysis

Besides the trend analysis within the cycle, every now and then it is is also worth to perform a trend analysis over a longer period of time, when sufficient data are available. In the last three years, or rather in the last three cycles, the ex-core measurements were made in R3, and there is sufficient data to perform a trend analysis. Stage 2018 lasted from mid-2018 to mid-2019, and only measurements from this period were analysed in the previous Stage. However, in 2018, there were two more measurements made, on 23 January and 24 April, which belonged to the cycle before Stage 2018 (cycle 35). These measurements were not evaluated before. Hence the trend analysis, performed with the refined method, actually stretches over the three cycles 35, 36 and 37.

The results of the the 3-year trend analysis for the beam mode are shown in Fig. 4.21. This figure shows the increase of the amplitude within the individual cycles, but it also indicates that there is a slow long-term increase of the amplitude. In particular the amplitude values at the end of the last two cycles for the lower detectors show a difference of about 50%. This can be an indication of the fact that

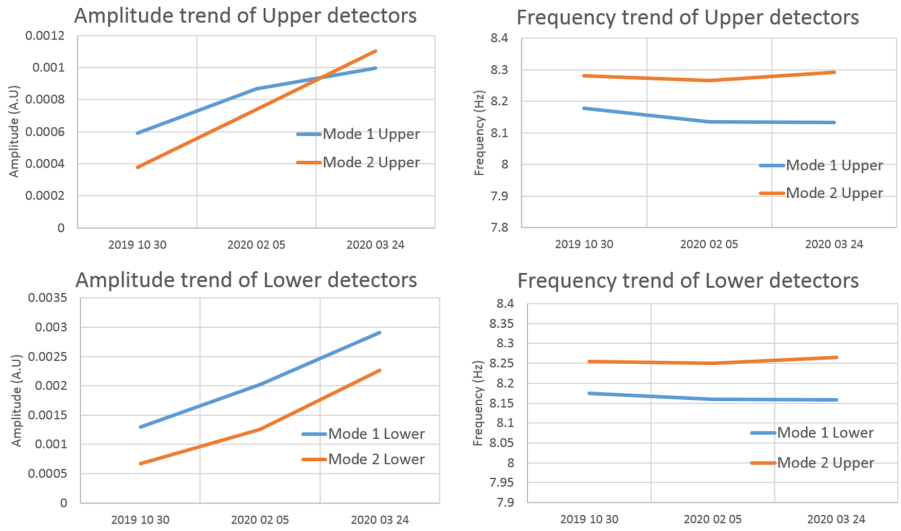

Figure 4.20: Trend analysis of the amplitude and frequency of the beam mode (Mode 1) and the reactivity component (Mode 2) at 8 Hz for the three measurements made during the cycle.

the play of the Lower Radial Key has increased. It will be interesting to follow up in the continuation whether this long-term trend continues, and if so, with which rate.

The same analysis for the reactivity mode, associated with the individual fuel assemby vibrations, is shown on Fig. 4.22. Here the behaviour is different. There is an increase between 2018 and 2019, whereas there is no increase after 2019, rather the amplitudes are generally lower. Since the fuel vibration properties may change after each new core loading, due to loading of fresh fuel and reshuffling of the remaining fuel assemblies, here a somewhat irregular trend behaviour could be expected. However, the amplitudes behave very similarly for the last two cycles.

It has to be noted that the trend analysis shown here was made for all three cycles wth the refined method. This means that the evaluation of the trend analysis of the measurements from the previous cycle, marked as "2019" in the above Figures, 4.22, does not correspond to the usual (within-the-cycle) trend analysis which was made earlier. It is thought that the new, refined method gives more reliable results. In particular, the somewhat puzzling non-monotonic behaviour of the amplitude of the reactivity mode (Mode 2) in the upper detectors, seen in the report of the previous Stage [13] is eliminated, and a monotonic behaviour is now seen in Fig. 4.22 for 2019. This also means that the results shown in this report for Stage 2018 deviate somewhat from those reported in the previous Stage.

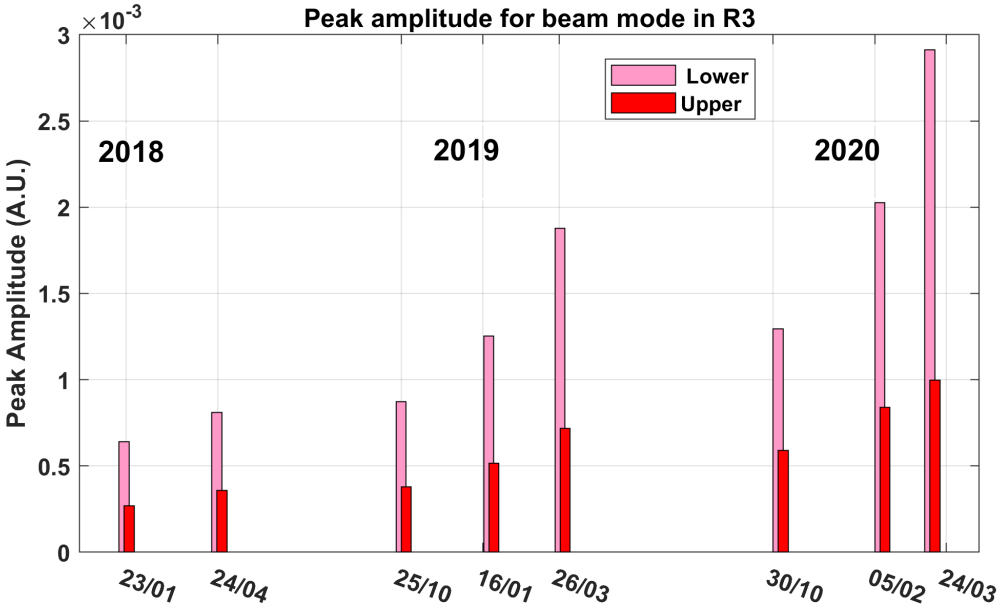

Figure 4.21: Three-year trend analysis of the amplitude of the beam mode (Mode 1) with the refined analysis method.

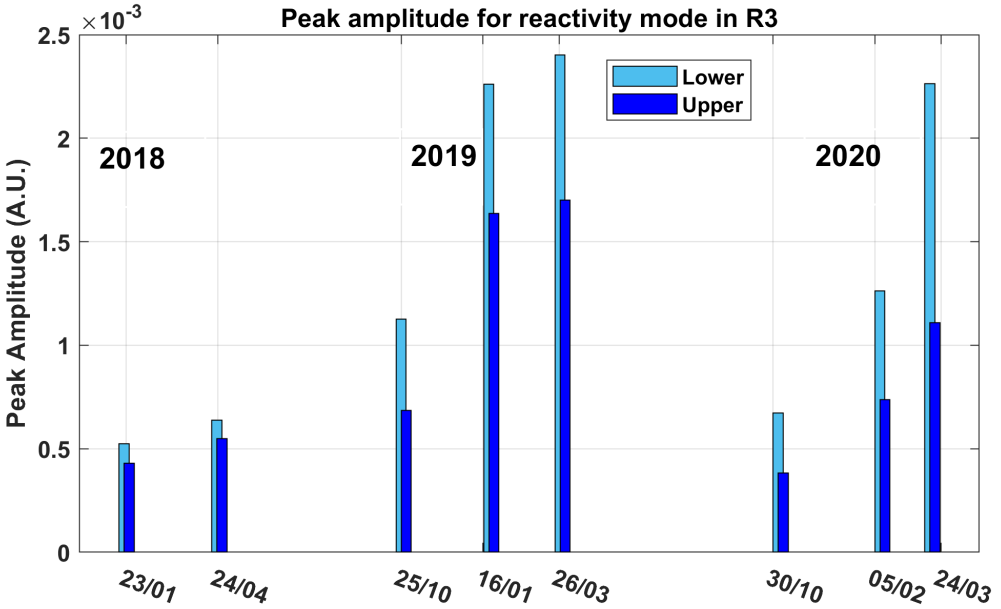

Figure 4.22: Three-year trend analysis of the amplitude of the reactivity mode (Mode 2) with the refined analysis method.

5. EXPERIMENTAL WORK AND SIMULATIONS IN SUPPORT OF THE USE OF FISSION CHAMBERS IN THE CURRENT MODE FOR REACTOR DIAGNOSTICS, AS AN ALTERNATIVE OF PULSE COUNTING METHODS

5.1 Introduction

In Stage 2016 [12] we suggested the possibility of using the continuous current of fission chambers to extract the same statistical information from a measurement as from the discrete events of pulse counting. Stochastic methods based on the statistics of pulse counting (variance to mean or Feynma-alpha and correlations, or Rossi-alpha) have traditionally been used for the determination of subcritical reactivity in low power systems, or in power plants during start-up. We suggested that the promtp neutron decay constant α, from which the subcritical reactivity can be extracted, can also be unfolded from the continuous signals of fission chambers, based on a newly developed theory of the statistical properties of fission chamber signals [17]. The advantage of the method would be that it is free from the so-called dead time problem, which prevents the application of pulse counting methods at high count rates, and therefore the application domain of the methods would be extended.

In Stage 2016 the basics of the theory were presented, and formulas were derived for the correlation method (Rossi-alpha) in a model without delayed neutrons [12]. In Stage 2018 this theory was extended to be applicable also to the Feynman-alpha method [13]. In both cases it was shown that, under certain conditions, the prompt neutron decay constant can be extracted from the statistics of the fission chamber signals.

To test the applicability of the theory, and to have a proof-of-principle of the method, one needs experimental verification. This was achieved by our collaborating partners at the Budapest University of Technology and Economics (BME, Hungary) and the Kyoto University Institute for Integrated Radiation and Nuclear Science (KURNS, Japan). Hence, in September 2019 a set of measurements has been performed on the Kyoto University Critical Assembly (KUCA) A-core in cooperation with the Institute of Nuclear Techniques of BME (BME NTI). One of the objectives of these measurements was the validation of the current mode noise analysis method for the determination of the subcritical reactivity. For this purpose, the voltage signals as well as time stamp data of detections in multiple detectors were recorded in different critical and subcritical configurations.

This summary provides an overview of the measurement configurations and instrumentation, as well as some preliminary results.

5.2 Core- and measurement configurations

The KUCA is a critical assembly, consisting of three different corse, designated as cores A, B and C. These cores are next to each other in the same reactor room, and only one of them can be operated at any time. The core A, on which the present measuremenrts were made, is a modular, solid moderated and reflected type core. The fuel is 93.2% enriched ^{235}U, embedded in aluminum alloy, in the form of 5.08 cm×5.08 cm×0.1587 cm metal plates. Assemblies are composed by placing fuel plates horizontally in rectangular aluminium tubes, alongside with polyethylene moderator blocks of similar dimensions. Due to their modular nature, assemblies can be arranged in a great variety of ways to fit the purpose of different experiments. Further details and parameters of the KUCA fuel-, moderator-, etc. assemblies, as well as the facility itself can be found in Ref. [18].

The configuration of the KUCA A-core, as used during the measurements, can be seen on Fig. 5.1, including the positions of four fission chambers (marked as *"A", "B", "C"* and *"D"*). This core has an excess reactivity of 0.170 %. Measurements were performed at critical state at three different power levels (Tab. 5.1), as well as two different sub-criticality levels (Tab. 5.2). Subcritical configurations were realized by different positioning of the three control rods. The reactivity-worth of each rod, related to this core configuration, is listed in Tab. 5.3.

Table 5.1: Power level of the KUCA A-core during the different critical measurements. Detector labels refer to the fission chambers where voltage signal data was recorded.

measurement name	power [W]	detector labels
CR-1	1.8414e-2	A, D
CR-2	1.8414e-3	A, D
CR-3	5.4648e-1	A, C

Table 5.2: Effective multiplication factor of the KUCA A-core during the different subcritical measurements, as well as the position of the control rods C1, C2 and C3. Detector labels refer to the fission chambers whose voltage signal data was recorded in a particular measurement.

measurement name	k_{eff}	detector labels	C1 position	C2 position	C3 position
SCR-1	0.9906	A, D	inserted	withdrawn	withdrawn
SCR-2	0.978	A, B, C, D	inserted	inserted	inserted

5.3 Instrumentation

During the measurements, two to four Westinghouse WL-8073 type dual-range fission chambers were used in the positions marked on Fig. 5.1, with ≈93% enriched ^{235}U as fissile material in the form of U_3O_8 compound. Individual detectors were placed in the same type of assembly-frame as other components of the KUCA core, with polyethylene padding at the top and bottom of the assemblies.

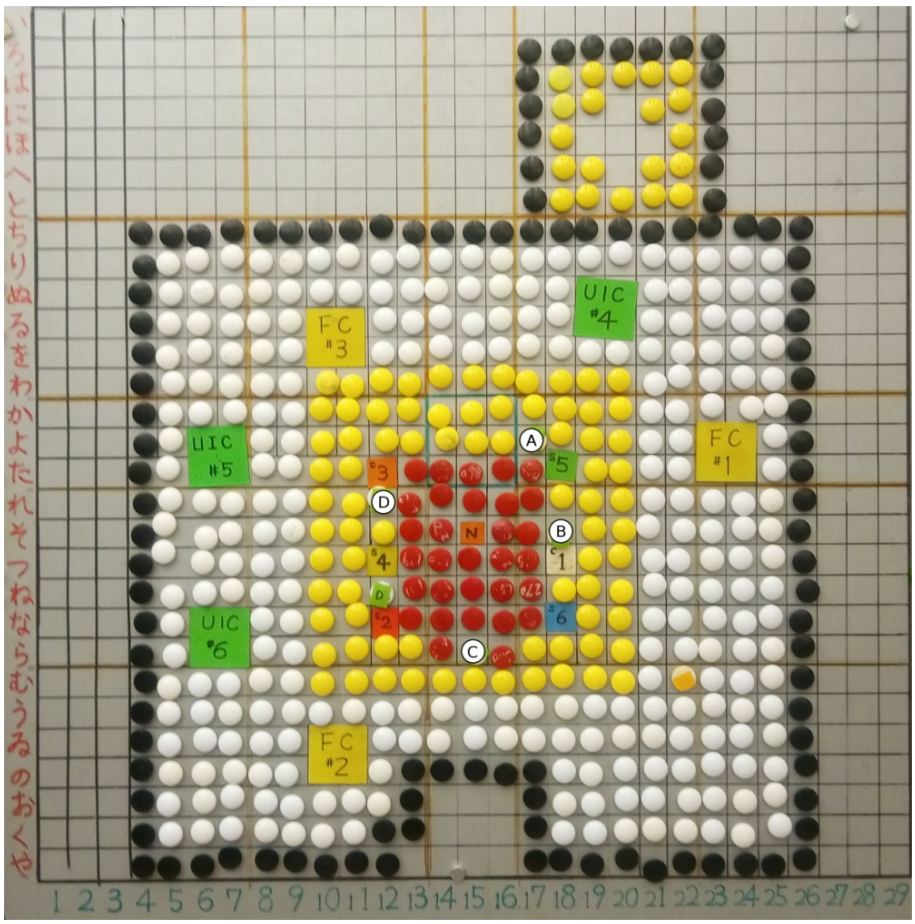

Figure 5.1: Layout of the KUCA A-core during reactivity measurements between 25-27 September 2019. Red pins refer to fuel assemblies; yellow pins refer to polyethylene moderator assemblies; white pins refer to polyethylene reflector assemblies; black pins refer to graphite assemblies. C1, C2 and C3 denote the control rods; S3, S4, and S5 refer to safety rods. Relevant detector positions are marked by A, B, C and D in white circles.

Table 5.3: Reactivity worth of the control rods 'C1', 'C2' and 'C3' in the core configuration used during current set of measurements.

rod	reactivity worth [%]
C1	1.117
C2	0.683
C3	0.588

The signal of each detector was sent to a separate, in-house-built high-frequency pre-amplifier which produced a voltage signal ranging between −1 and 1 V (Ref. [19]). The pre-amplifier circuit has a small time constant (compared to the charge collection time of the detector), hence the shapes of the amplified voltage pulses reflect the shapes of the current pulses in the detector. The voltage signals of the four detectors were then digitized by a pair of Red Pitaya STEMLab 125-14 type FPGA-based A/D converters ([20],[21]). Each converter has two analogue inputs and provides a 14 bit vertical resolution as well as 125 MHz maximal sampling frequency (corresponding to a 8 ns maximal resolution in time). The digitized amplitude values were then recorded to binary files on a computer. Fig. 5.2 displays a schematic layout of the instrumentation used in the measurements.

During the measurements, time stamp data were recorded using a NI-myRIO device, employing a software developed in BME NTI Ref. [22]. Data analysis related to this recording method is not included in this report.

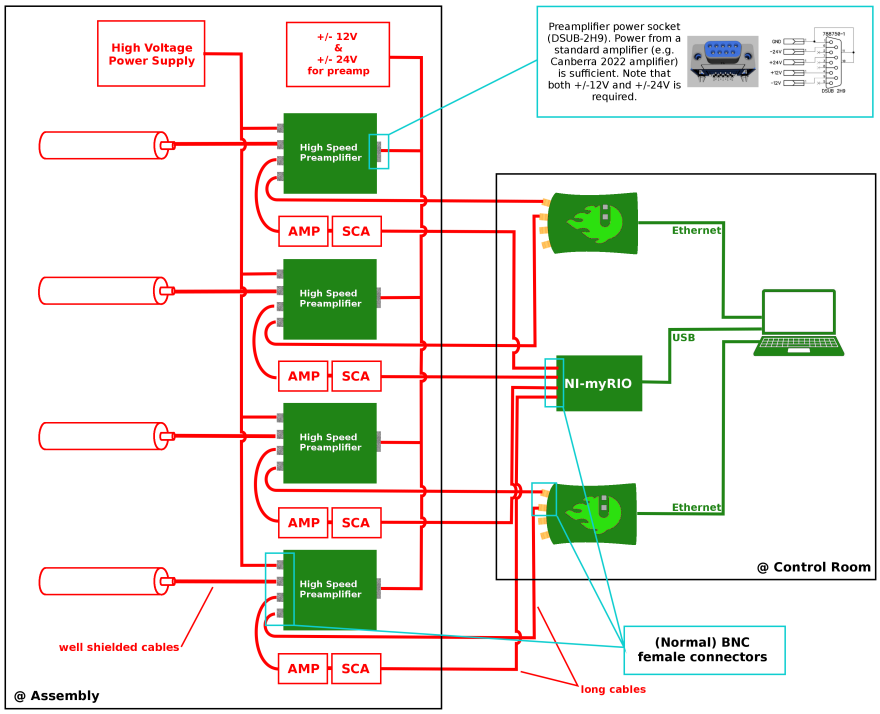

Figure 5.2: Schematic layout of the instrumentation used in the measurements between 25-27. September 2019. Pre-amplifiers were located close to the detectors near the KUCA A-core, while data-recording devices were located in the control room of the facility.

5.4 Principles of the analysis

One of the frequently used methods for estimating the prompt neutron decay constant α in a multiplying system, which contains the sought subcritical reactivity ρ, is the auto-covariance method, or Rossi-α method. When applying this method in its traditional form, the auto-covariance of the neutron pulses is determined Ref. [23]

around two time instants t_1 and $t_2 = t_1 + \tau$. A detailed theoretical calculation of the value of this covariance can be found in e.g. Ref. [23]. Here we only provide the simplified form of the case when the effect of delayed neutrons is neglected, which reads as

$$\mathrm{Cov}(\tau) = a\,\mathrm{e}^{-\alpha\tau} + b. \tag{5.1}$$

In the above equation α denotes the prompt neutron decay constant, whereas a and b are constant parameters (whose definitions can be found in Ref. [23]). This formula shows that if the auto-covariance function of the number of detected counts is estimated, the prompt neutron decay constant can be extracted by fitting a function of the form (5.1) to the measured auto-covariance.

In Stage 2016, an alternative form of the Rossi-α method was developed [12, 24], based on a stochastic model of fission chamber signals, Ref. [17]. According to this new method, the covariance of the time resolved current or voltage signal of the neutron detector at two time instants t_1 and $t_2 = t_1 + \theta$ is determined. By omitting the details of the lengthy theoretical calculations which are found in [12], the final form of the covariance can be written as

$$\mathrm{Cov}(\theta) = c\,\mathrm{e}^{-\alpha\theta} + f(\theta)\,\mathrm{e}^{-\alpha_e\theta}. \tag{5.2}$$

Here the notation of the time lag was changed to θ, in order to be consistent with the notations in the report for Stage 2016 [12], as well as with Ref. [24]. The exact form of the coefficients c and $f(\theta)$ are found in Eq. (7.64) of Ref. [12] (note that f also depends on the time lag θ, containing terms linearly increasing in θ); α is the prompt neutron decay constant, whereas α_e is a decay constant of the shape of the detector pulse, induced by the detection of a neutron.

Clearly, expression (5.2) shows a resemblance to the covariance function (5.1) of the traditional Rossi-α method; however, it is much more complicated due to the second term. In particular, the additional term $f(\theta)\,\mathrm{e}^{-\alpha_e\theta}$ is not only dependent on the time lag θ, it even contains an exponentially decaying term, similarly as the first term, from which the prompt neutron decay constant α is to be determined. For thermal reactors, α and α_e are very well separated, irrespective of the measure of the subcriticality of the system. In general, $\alpha_e >> \alpha$, i.e. the exponential in the second term decays much faster than the first. In such cases α can be readily determined from the measurement. On the other hand, if $f(\theta) >> c$, the second term of (5.2) dominates, hence it is difficult to extract the prompt neutron decay constant α from the measurement.

However, it was shown in Refs. [12, 24] that when the multiplying system is not too far from criticality, the first term will dominate over the second one, and the covariance function can be approximated as

$$\mathrm{Cov}(\theta) \approx c\,\mathrm{e}^{-\alpha\theta}. \tag{5.3}$$

This formula suggests that the prompt neutron decay constant can again be extracted from the estimated covariance function of the detector signal by fitting a function of the form (5.3).

5.5 Data analysis

As mentioned previously, our goal was to demonstrate the estimation of the prompt neutron decay constant from the time resolved signals of the detectors. In order to validate the method, a direct comparison with the pulse counting technique was needed. The only way of doing this was to perform an experiment, in which both methods are applicable. With overlapping pulses, the pulse counting technique fails, due to the presence of the dead time. On the other hand, the analysis of the time-resolved current (voltage) of the fission chambers is valid both for individual (non-overlapping) as well as overlapping pulses.

Therefore, the measurements were performed on configurations where the detection rate was so low that the overlap of pulses was expected to be insignificant. This condition is fulfilled in subcritical configurations not too close to criticality, considering the intensity of the available neutron source. On the other hand, measurements have also been performed in the critical configuration at several power levels (see in Table 5.1) in order to do the comparison with pulse counting at low count rates and test also the method at higher count rates. Evaluation of these latter measurements is still in progress.

This, in turn, made it possible to calculate the autocovariance function both with the traditional pulse counting approach as well as with the newly proposed method of analyzing the continuous detector signals, in order to assess the performance of the new method. Nevertheless, one trick was necessary to employ in order to make the decay constant values more comparable. Namely, the traditional Rossi-α method was not applied to the time stamp data collected on-line with the use of multi channel analysers; rather, the continuous signals were analyzed off-line by a computer program, and the pulses were counted at an appropriate threshold level. Naturally, one would not use such a laborious method in practical applications; however, our goal here was the validation of the fission chamber signal-based method, for which we wanted to ensure a complete equivalence of the data to be analysed. Measurements have also been carried out in configurations with high detection rates, where the dead-time effect is expected to be more significant in case of the traditional Rossi-α method, but there the purpose was to see the expected differences in the results, based on the fact that the pulse counting method is affected by the dead time, whereas the method based on the continuous signals of fission chambers is not.

As it can be expected, high frequency electronic noise was superimposed on the recorded signals. In order to investigate its effect on the estimated values of the prompt neutron decay constant, smoothed versions of the signals were produced and analyzed off-line as well. The signals were smoothed using a simple moving average algorithm, where each data point was substituted with an unweighted average of 21 consecutive points (lying symmetrically around the original data point). In case of 40 ns and 48 ns time resolutions this resulted in 0.84 μs and 1.008 μs long averaging windows, which are long enough to suppress most of the high-frequency electronic noise, but sufficiently short not to distort the shape of the pulses very much. On Fig. 5.3 the effect of the smoothing is illustrated on a short signal segment.

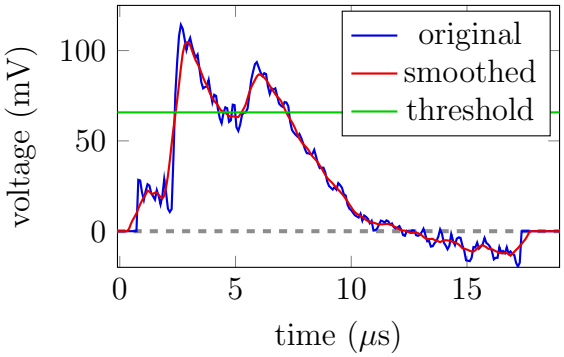

Figure 5.3: Illustration of signal smoothing with a simple moving average algorithm.

We found that suppressing the electronic noise had a negligible effect on the covariance function obtained from the continuous signals. This is the result of a known property of the covariance function: as a second order moment, it suppresses small amplitude uncorrelated signal components such as the electronic noise. On the other hand, the electronic noise produced a considerable number of false counts in the pulse counting approach, which were, however, successfully eliminated by smoothing. This lead to the conclusion that the analysis of the time-resolved detector signals was insensitive to the electronic noise; application of the smoothing was required only to get the correct detection rates from pulse counting. Nevetheless, for better visibility, in the remainder of this report, results are presented only for smoothed signals.

In our evaluated measurements so far, the cases considered consist of estimation of the Rossi-α with two different approaches for the two subcritical configurations. The time resolution of the data obtained from measurements SCR-1 and SCR-2 is 40 ns and 48 ns respectively. Fig. 5.4 illustrates the results of the data analysis for detector A in case of the second subcritical configuration (SCR-2), and Tab. 5.4 lists all estimated α values obtained from the Rossi-α analysis. The results show good agreement between values obtained from the voltage signal analysis and the pulse counting methods in case of the SCR-2 configuration. In case of the SCR-1 configuration, which is closer to the critical state, a more significant difference can be observed between the corresponding α-values. This is suspected to be caused by the higher count rates and dead-time effect in the detectors. Further analysis is required regarding this matter.

5.6 Conclusions and further plans

The preliminary results reported here suggest that the value of the prompt neutron decay constant α can be reconstructed from the time-resolved signals of fission chambers. The measurement made it possible to estimate the Rossi-α also with the traditional pulse counting method, and a good agreement between the two methods was found.

The work in this field will continue on several lines, and will be included in the next Stage. The analysis and interpretation of the already existing data from the

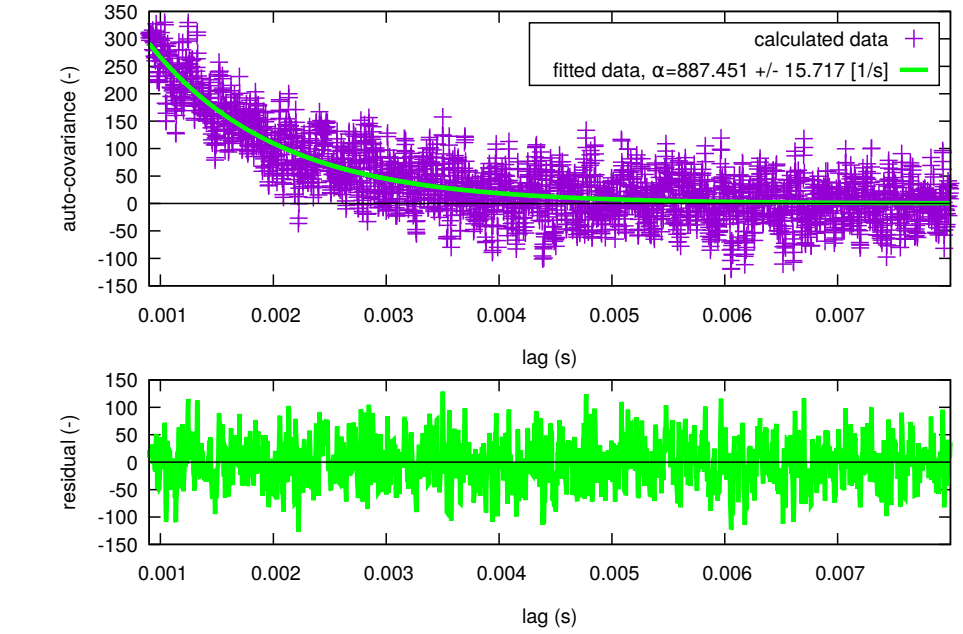

(a) Auto-covariance function of the voltage signal data.

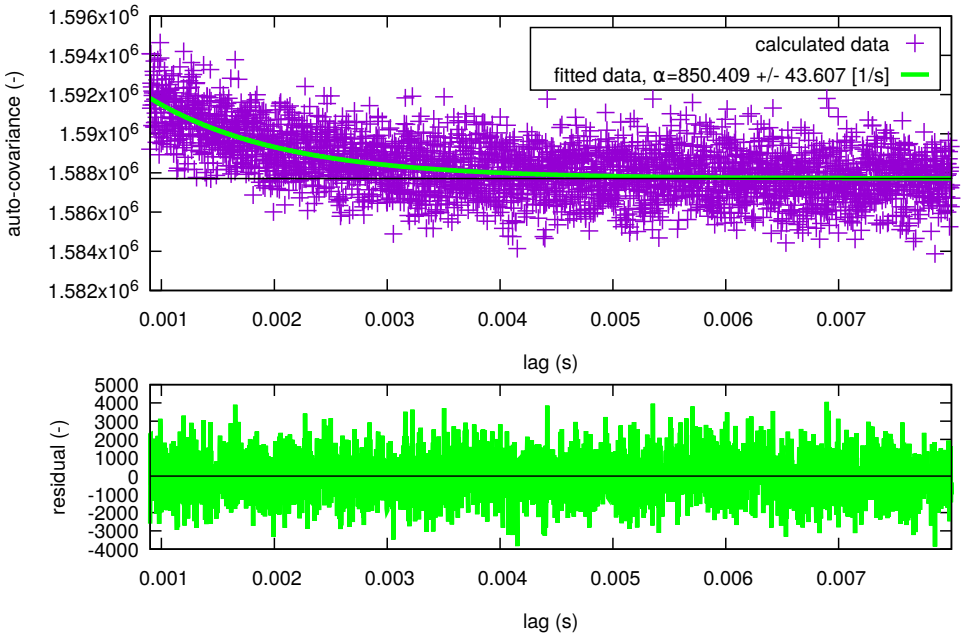

(b) Traditional auto-covariance of the time stamp data.

Figure 5.4: Results of the two different approaches for Rossi-α evaluation for detector A in case of the SCR-2 configuration.

Table 5.4: Estimated α values from the Rossi-evaluation for the subcritical configurations, and measured count rates of the individual channels.

Configuration	Detector pair	$\alpha_{signal\ analysis}$ [1/s]	$\alpha_{pulse\ analysis}$ [1/s]	*count rate* [1/s]
SCR-1	A-A	664.168±11.2095	579.7±29.026	21759.9±137.8
	D-D	648.339±10.2155	525.2±25.885	19948.2±130.4
SCR-2	A-A	887.451±15.717	850.4±43.607	8573.6±89.4
	B-B	814.113±19.744	777.4±59.676	4465.5±66.0
	C-C	960.608±14.563	935.2±35.768	9945.4±95.6
	D-D	910.573±25.305	1010.9±84.079	3904.0±62.6
	A-B	999.596±18.106	927.3±41.610	
	C-D	1009.953±18.065	945.2±38.716	

measurements, made in critical conditions at KUCA and at the BME Training Reactor, will be completed. Further, the data analysis in order to apply the Feynman-α method with time resolved fission chamber signals will also be made. Finally, new measurements are planned both at the BME Training Reactor and at the KUCA reactor on other configurations, to increase the extent of the validation procedure. One interesting aspect would be to investigate the applicability limits of the fission chamber-based analysis method for higher core power (neutron flux) leading to fully overlapping detector pulses, when the pulse counting method is definitely not applicable. Such an experimental scenario will be possible to investigate up to 100 kW power at the BME Training Reactor.

6. DEVELOPMENT OF A NEW METHOD TO DETERMINE THE AXIAL VELOCITY PROFILE OF THE VOID IN THE CORE OF A BWR BY USING FOUR PERMANENT IN-CORE LPRMS AND A TIP DETECTOR

6.1 Introduction

Determination of the local void fraction in BWRs from measurements with existing instrumentation has been a matter of interest for a long time. Although several suggestions were put forward during the years concerning how to extract the local void fraction from in-core neutron noise measurements [25, 26], the suggested methods were incomplete and required either calibration, or several auxiliary conditions, whose fulfilment was unclear and rather uncertain, or both.

The question of experimental determination of the local void fraction was taken up also in Stage 13 of this project [8]. A conceptual study was made to investigate the applicability of two indicators: a) the normalised root mean square (NRMS) of the individual detector spectra in the frequency range 3 - 12 Hz, and b) the upper break frequency of the APSDs. Only the NRMS was investigated quantitatively, and only the existence of a relationship between the NRMS and the local void fraction was shown. No underlying theory is available which could expedite the extraction of the quantitative value of the void fraction either from the NRMS or from the break frequency.

To make progress, in Stage 14 we investigated how the void velocity at the detector positions could be utilized either by using a direct relationship between the void fraction and the void velocity through mass conservation and a slip ratio assumed being equal unity, or from a relationship between the break freqency on the one hand, and the void velocity and the local value of the spatial range of the local component of the neutron noise. A bubbly flow was simulated through a Monte-Carlo simulation, with the help of which the performance of the above two methods could be investigated in model cases [9, 27]

The above methods both are based on the assupmtion that the local void velocity is known at the neutron detector positions. However, in in-core noise measurements only the transit times of the void between two axially displaced neutron detectors can be obtained. The transit times are integrals of the inverse of the velocity, which is not constant between the detectors. The relationship between the void velocity at the detector positions, and the transit time between the detector pairs, is hence rather involved.

Determination of the void velocity at the detector positions requires the reconstruction of the whole axial velocity profile. Since the axial depencence of the velocity has an inflection point, it has to be described by a non-linear function. The simplest such function, which was also suggested in [27] and [9], and which is the only one tested so far, is a third order polynomial. However, the use of such a

functional form of the velocity profile met difficulties.

The main problem arises from the fact that a third order polynomial has four parameters. To determine these, one would need four independent transit times, hence access to five detectors. The standard instrumentation of BWRs comprises only 4 detectors axially at one radial core position, hence one has access to three transit times between the three detector pairs.

To solve this problem, it was suggested that one could use, in addition to the four standard LPRMs, a TIP detector, and make a measurement at an axial position either between the four LPRMs, or outside these, i.e. in a position different from those of the LPRM positions. This approach was tried in measurements, performed in the Swedish Ringhals-1 BWR [10]. Unfortunately, as is also described in [10], the attempt was unsuccessful. Due to the fact that the data acquisition for the LPRMs and the TIP detectors is made by different equipment with different buffering properties, the data acquisition for them was not completely synchronouos. There is the further difficulty of the inaccuracy of the positioning of the TIP detectors. The conclusion in [10] was that the application of the TIP detector for acquiring a fourth transit time is not feasible.

Therefore, in this Stage we suggest a different strategy. First, we realise that there is no need for a fourth transit time to determine four parameters of velocity profile, either a polynomial or some other form, if the axial point of the onset of the boiling is known. The onset point of the boiling can be determined with a TIP detector alone, from the amplitude of its root mean square noise (RMS) or its APDS, or, alternatively, from the coherence between the TIP and the lowermost LPRM, if these are determined as a function of the axial position of the TIP. At the onset of the boiling the void velocity can be assumed to be equal to the inlet coolant velocity, which is known, Thus, knowledge of these two quantities reduces therefore the number of unknowns of the axial velocity profile to be determined from four to three.

Second, there exist non-linear functions with an inflection point, which represent an even higher order non-linearity than a third order polynomial, but which nevertheless can be parametrised with only three parameters instead of four. Examples are certain trigonometric or sigmoid functions. For simplicity these profile types will be referred to as 'trignometric". In this case not even the onset point of the boiling needs to be known; determination of the void profile is then possible based on solely of the three measured transit times with the standard instrumentation, without the need for using a TIP detector at all.

In the following the principles, as well as the applicability of both types of velocity profile forms (trigonometric and polynomial) will be investigated in conceptual studies. Various types of velocity profiles will be assumed, both trigonometric and polynomial), will be assumed as the "true" profiles as a starting point. From the true profiles, the three transit times between the four detectors can be calculated, and then the inversion procedure applied and its accuracy investigated. Since we do not have access to measurement data with four transit times or three transit

times plus the knowledge of the axial onset point of the boiling, we need to make some assumptions when investigating the applicability of the polynomial form. The sensitivity of the results on the accuracy of these assumptions will be illustrated in model calculations. We will also investigate the flexibility of the two forms of the velocity profiles to reconstruct various types of axial velocity dependences, and the sensitivity of the reconstruction on the correct assumption on the form of the profile (i.e. starting with a trignometric as "true" and performing the reconstruction with the polynomial form, and vice versa), as well as taking a true polynomial profile with a given onset point of the boiling and making the reconstruction with a different onset point as an incorrect guess. Finally, an attempt will be made to reconstruct the (unknown) velocities at the detector positions from a measurement at Ringhals-1, both with the trigonometric and the polynomial velocity forms. The focus of the investigation is to see which method can reconstruct the known transit times better, and which inversion method is more robust and convergent.

6.2 The velocity profile and its modelling

6.2.1 Characteristics of the velocity profile

As is general in reactor noise diagnostics problems, when only a limited number of measurements is available, obtained from detectors in a few specified spatial positions, it is not sufficient to reconstruct the full spatial dependence of the noise source. Inevitably, one needs to make an assumption on the space dependence of the noise source in an analytical form, which contains only a limited number of free parameters. These can then be determined from the limited number of measurements [28].

This strategy is easy to follow for localised perturbations, such as a local channel instability or the vibrations of a control rod, since the perturbation can be simplified to a spatial Dirac-delta function, either with a variable stength, or with a variable position. All these cases can be described by a few parameters, whose physical meaning is obvious, and the guess on the analytical form is rather straightforward. What regards the reconstruction of the velocity profile, the case is more complicated. Here a whole profile (the axial dependence of the velocity) needs to be reconstructed, and it is not obvious how to parametrize it. The main difficulty is that, for obvious reasons, no directly measured velocity profiles are available, which would give a definite hint. Only qualitative information is known either from calculations with system codes, from common sense considerations, or from simulations.

An inventory of the available knowledge yields the following. What regards results from calculations with system codes, we have some data from TRACE and RAMONA calculations. Fig. 6.1 shows a few profiles from calculations with TRACE, where account was taken for the fact that the boiling does not start at the inlet, rather at a higher elevation (courtesy of Mathieu Hursin, EPFL/PSI, Switzerland). On Fig 6.2, calculations with RAMONA of the steam velocity in Ringhals 1 in a few selected channels are shown. In this latter, the discontinuity at around 2.5 m is due to the fact that the fuel assemblies, in which the calculations were made, contain partial length fuel rods. At this elevation, there is an abrupt change in the

void/fuel ratio, hence the sudden change in the void velocity. Such effects were not taken into account in the present analysis; taking into account their existence would necessitate further development of the method.

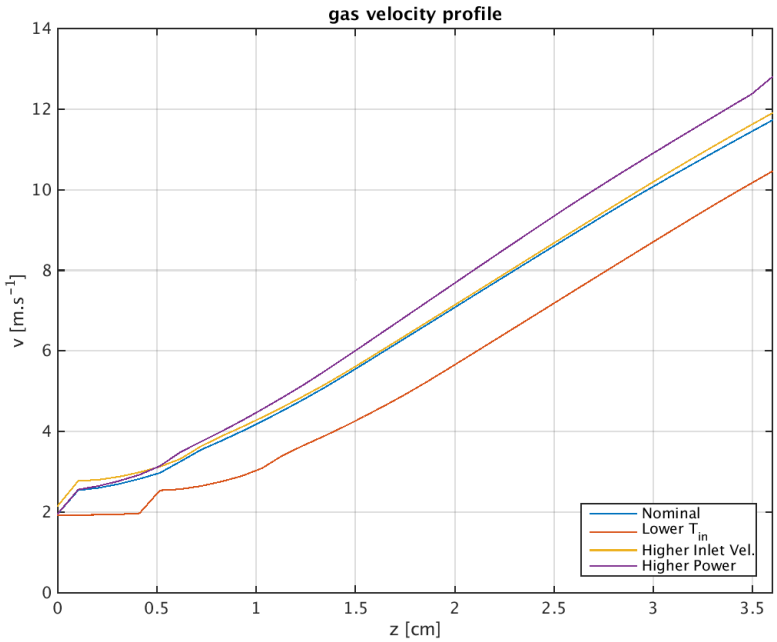

Figure 6.1: Void velocity profiles simulated by TRACE

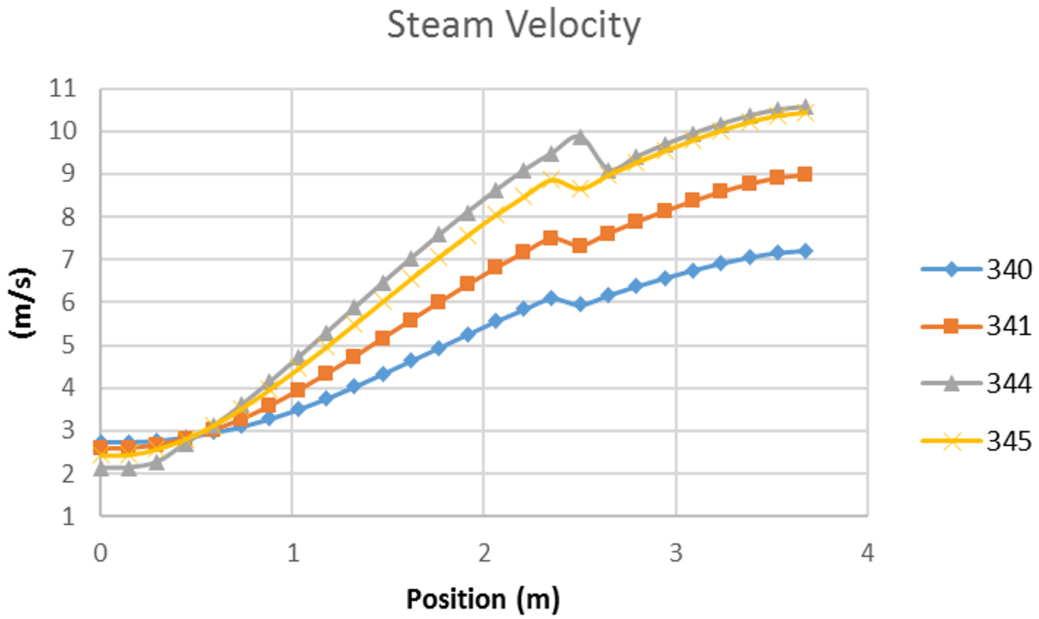

Figure 6.2: Void velocity profiles simulated by RAMONA in channels 340, 341, 344 and 345

Another possibility is to use results from simulations of a bubbly flow in a heated channel, which were performed by an in-house Monte Carlo code. This code was developed earlier in Stage 14 [9], and used in previous work. Some profiles, resulting from these simulations, are shown in Fig. 6.3.

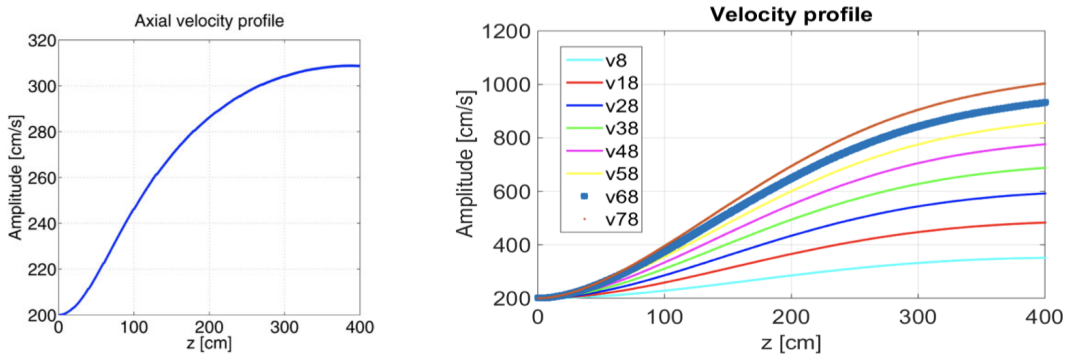

Figure 6.3: Void velocity profiles simulated by a Monte-Carlo model of bubbly two-phase flow

What these figures tell us is that the velocity increases monotonically in the channel from the inlet, first at least quadratically, then the increase slows down, either leading to an inflection point, or to a linear increase towards the core exit. Apparently, to find out the best analytical form of the axial velocity profile, a much wider data base should be available for each different reactor construction. This data base is though yet to be constructed.

6.2.2 Possible analytical forms

In our previous works [9, 10, 27] a third order polynomial was assumed:

$$v(z) = a + b\,z + c\,z^2 + d\,z^3 \tag{6.1}$$

This form has found to have some disadvantageous properties: partly that the integral of $v^{-1}(z)$ w.r.t. z does not exist in an analytical form, and partly that it assumes that the boiling starts at the inlet, i.e. at $z = 0$, which is not true in practical cases.

The first of these disadvantages does not represent a significant difficulty, since the unknown parameters a - d can also be determined by numerical unfolding methods, as it will be shown below. Even for the trigonometrical profile, where the same integral exists in analytical form, the numerical unfolding method is more effective than root finding of a highly not-transcendental analytical function in several variable.

The second property poses somewhat larger problems. Accounting for the fact that the onset of the boiling is at $z = h$ where h is an unknown, would increase the number of parameters to be determined to 5. However, as suggested in this work, if the onset point $z = h$ of the boiling is known from measurements, then the third

order polynomial form of (6.1) can be written in the form

$$v(z) = \Delta(z-h)\,\left[v_0 + b\,(z-h) + c\,(z-h)^2 + d\,(z-h)^3\right] \tag{6.2}$$

where $\Delta(z)$ is the unit step function, and v_0 is the (known) inlet coolant velocity. This form contains only three unknowns, which can be determined from the three measured transit times. This procedure is suggested for future use, such that the onset point of boiling is determined by measurements with movable TIP detectors.

Since such measurements are not available at this point, the test of the polynomial form will be made such that a guess of the onset point will be made. One can assess the uncertainty of the unfolding procedure with a polynomial profile with respect to the error in the estimation of the position of the onset point of boiling.

In addition in this Stage we propose also to investigate another path. The essence is the recognition that there exist non-linear functions other than a third-order polynomial which have an inflection point, and which contain only three free adjustable parameters. These include trigonometric functions, such as $a \cdot \mathrm{atan}\,(b\,(z-c))$, where a, b and c are constants, or the co-called "sigmoid" function, used in the training of ANNs. In the continuation we will refer to such profiles as "trigonometric". For such profiles the onset point of the boiling does not need to be known. In the next section such a model is proposed, and a procedure for its use for the unfolding of the velocity profile is suggested.

Of course, the price one has to pay for the convenience of only needing to fit three parameters instead of four is that the structure of the profile is more "rigid" than that of the more general polynomial form, hence its flexibility of modelling and reconstructing a wide range of velocity profiles is reduced as compared to the polynomial fitting. If the onset point of boiling was known, then clearly the polynomial profile would be recommended. It the onset point is not known, it is not clear whether the use of a trigonometric form, or that of the polynomial form used with a guess for the axial point of the onset of the boiling yields better results.

6.3 Construction of a simple non-polynomial velocity profile

In order to obtain a velocity profile with an inflection point, which can be described by a few parameters, we shall assume a very simple phenomenological model based on simple considerations. The model does not have any deep physical meaning, or justification. One of its advantages, besides its simplicity, is that since it is based on a physical model, it makes is simpler to estimate the possible range of the model parameters (which is useful in the inversion process), and in particular it is more straightforward to find initial guesses of the parameters included to the numerical inversion procedure than for the polynomial model. Although, the comparative investigations made later on in this chapter will show that this latter advantage is not significant in the sense that the polynomial model is much less sensitive to the correct choice of the starting guess of the sought parameters than the non-polynomial model.

Assume that the core boundaries lie between $z = 0$ and $z = H$ in the axial direction with a static flux $\phi(z)$. Assuming that the boiling starts at the axial

elevation $z = h$, and that there is a simple monotonic relationship between void fraction and void velocity, and that the latter at point z is proportional to the accumulated heat production between the boiling onset and the actual position, gives the form

$$v(z) = \Delta(z-h)\left\{v_0 + c\int_h^z \phi(z)\,dz\right\}. \tag{6.3}$$

where h and c are unknown constants[1]. Assume now, for simplicity, a simple cosine flux shape as

$$\phi(z) = \cos[B(z - H/2)] \tag{6.4}$$

In reality, the axial flux shape in a BWR deviates quite appreciably from a cosine-shaped profile, and moreover that profile is known from in-core fuel management calculations. Hence, the assumption of the simple cosine flux profile could be replaced with a more realistic one, although presumably at the price that the simplicity of the model, and hence its advantages, would be lost. This question will be investigated in the next Stage.

In Eq. (6.4) it is not assumed that $B = \pi/H$, rather B is kept as an independent (unknown) parameter. By allowing $B < \pi/H$, the effect of the reflector, represented as an extrapolation length as an independent parameter, can be accounted for.

With this choice, after integration, the velocity profile is obtained in the simple form

$$v(z) = \Delta(z-h)\left\{a_1 + c_1 \sin\left[B\left(z - \frac{H}{2}\right)\right]\right\} \tag{6.5}$$

with

$$a_1 = v_0 - \frac{c}{B}\sin\left[B\left(h - \frac{H}{2}\right)\right] \quad \text{and} \quad c_1 = \frac{c}{B} \tag{6.6}$$

A qualitative illustration of a typical velocity profile provided by this model, referred to as the trigonometric profile, is given below. To this order, geometrical as well as inlet and outlet velocity data are taken from the Ringhals-1 plant. The geometrical arrangement is depicted on Fig. 6.4, giving the core height and the axial positions of the detectors from the core bottom. The 4 fixed LPRM position are marked on the left, whereas the 7 intermediate positions where TIP detector measurements were made and tried to be used in Stage 14 to generate extra transit times, are marked on the right. In the present study only the LPRM positions will be used. The inlet coolant velocity is $v_{in} = v_0 = 2$ m/s, and the outlet void velocity is about 12 m/s. Assuming an extrapolation distance of 0.2 m for the flux, and assuming the onset of the boiling at h =0.2 m, the static flux and the arising velocity profile are shown in Fig. 6.5.

This simple model will be tested in model problems, together with the polynomial profile, as well as in an attempt to reconstruct the velocity profile from a Ringhals measurements.

[1]As mentioned earlier, if needed, h can be determined by measurements with a TIP detector.

6.4 The unfolding procedure

First we tried to use the velocity profile given in Eq. (6.5), since it depends only on three parameters, hence three transit times, derived from four LPRM signals, should be sufficient for reconstucting the velocity profile. Eq. (6.5) has the further property that its inverse is analytically integrable, thereby giving a possibility to express the transit time $t_{1,2}$ of the void between the detector positions z_1 and z_2, with $z_1 < z_2$, as analytical functions of the unknown parameters a_1, c_1 and B. For practical reasons we will number the detector positions such that z_1 corresponds to

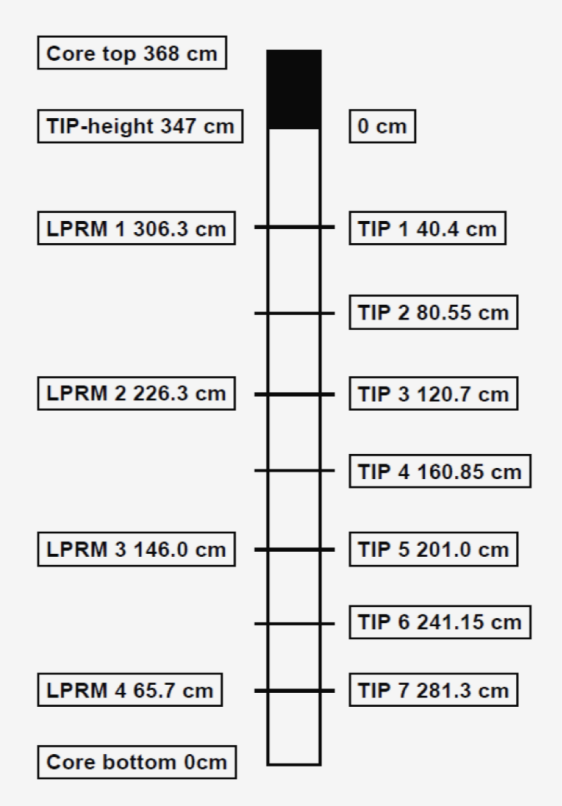

Figure 6.4: Layout of the measurements

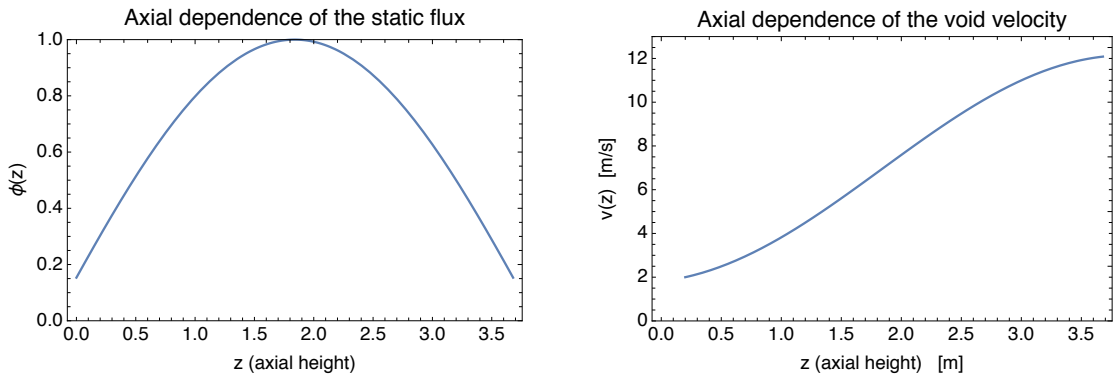

Figure 6.5: Flux and void velocity profile

the lowermost detector, LPRM 4, and the transit times between the detector pairs will be indexed by the position of the lower detector, i.e. $t_{1,2} \equiv t_1$ etc.

With these notations, one has

$$t_i(a_1, c_1, B) = \int_{z_i}^{z_{i+1}} \frac{dz}{v(z)} =$$

$$\frac{2\left(\tan^{-1}\left(\frac{c_1 - a_1 \tan\left(\frac{1}{4}B(H-2z_{i+1})\right)}{\sqrt{a_1^2 - c_1^2}}\right) - \tan^{-1}\left(\frac{c_1 - a_1 \tan\left(\frac{1}{4}B(H-2z_i)\right)}{\sqrt{a_1^2 - c_1^2}}\right)\right)}{B\sqrt{a_1^2 - c_1^2}} \tag{6.7}$$

Our expectation was that in possession of the analytical expressions for $t_i(a_1, c_1, B)$, $i = 1, 2, 3$ in the above form, and having access to given values of the three measured transit times $\tau_i,\ i = 1, 2, 3$, the unknown parameters a_1, c_1, B can be determined as the roots of the non-linear equation system

$$t_i(a_1, c_1, B) = \tau_i, \qquad i = 1, 2, 3 \tag{6.8}$$

This strategy was tested by choosing detector positions, core size, as well as inlet coolant velocity and the same value for c_1 which were used in calculating the profile in the right hand side of Fig. 6.5. Having the analytical form of $v(z)$, the concrete transit times $\tau_i,\ i = 1, 2, 3$ can be numerically evaluated and used in (6.8), with the t_i given in the analytical form (6.7). For the numerical solution of this non-linear equation system, the numerical root finding routine `NSolve` of Mathematica 12.0.0.0 was used [29]. However, the root finding did not converge, even if quite accurate starting values were specified. It appears that the `NSolve` routine is primarily designed for treating polynomial equations, rather than transcendental ones.

Therefore, another path was followed to unfold the parameters of the void profile from the transit times. Instead of using `Nsolve`, a kind of fitting procedure was selected by searching for the minimum of the penalty function

$$\sum_i^3 \left[t_i(a_1, c_1, B) - \tau_i\right]^2 \tag{6.9}$$

as functions of a_1, c_1 and B. First the `FindMinimum` routine of Mathematica, was used. This procedure worked well and was able to reproduce the input parameters of the velocity profile. Initially the analytical form (6.7) was used for the $t_i(a_1, c_1, B)$. However, it turned out that defining these latter as numerical integrals with free parameters a_1, c_1, B worked much faster and with better precision, showing also that for the unfolding, it is not necessary that the transit times are given in an analytical form. Consequently, the modified polynomial form of $v(z)$ in Eq. (6.2) can also be used, despite that $v^{-1}(z)$ is not integrable analytically.

The unfolding procedure was tested using both the trignometric velocity profile given in (6.5), as well as with the polynomial profile of Eq. (6.2). Tests were made with various values of the parameters, also with combinations that yielded velocity

profiles similar to those in Fig. 6.1. These extended numerical tests were made by Matlab, using the `fsolve` routine to find the minimum of the penalty function.

6.5 Test of the reconstruction algorithm

6.5.1 Trigonometric profile

Two tests will be shown for illustration, with two different profiles. We used a more curled and flatter profile, respective, with the following data:

1. H = 3.68 m; d = 0.2 m; h= 0.2 m; c = 4; v_0 = 2 m/s.
2. H = 3.68 m; d = 0.8 m; h= 0.2 m; c = 3.6; v_0 = 2 m/s.

The true (=starting) and reconstructed profiles for these two cases are shown in 6.6. The solid red line represents the true profile, and the broken blue the reconstructed one. It is seen that the inversion algorithm was able to reconstruct the original profiles in both cases quite well.

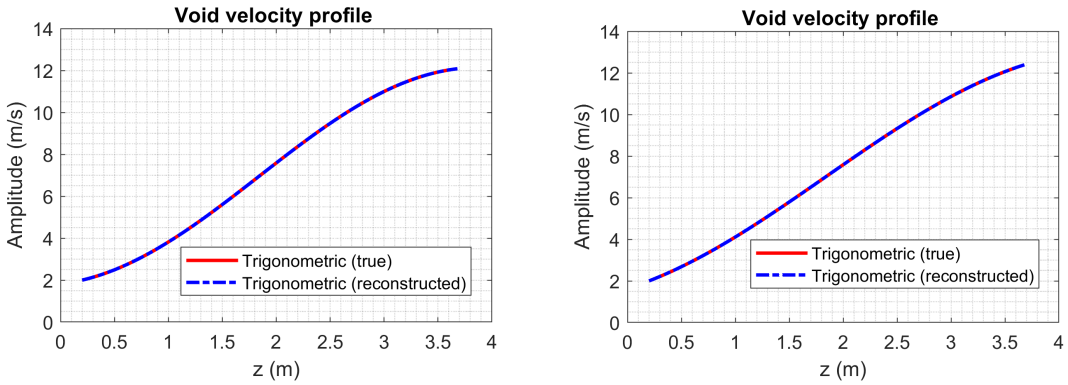

Figure 6.6: Reconstruction of two trigonometric velocity profiles

Tests made on a large variety of different profiles revealed that finding the minimum of the penalty function, (6.9), with the Matlab routine `fsolve`, the procedure in some cases did not converge to the true parameters. In some cases the minimum searching ended up by providing complex numbers for the searched parameters, even if quite accurate starting values and searching domains were specified. This lack of convergence is a reason for concern, since in a real application one does not know the searched parameters and hence cannot specify good starting values. However, the fact of sometimes obtaining complex values of a_1, c_1 and B gave the idea of taking only the real part of the search function, such that the minimizition was performed on the modified penalty function

$$\sum_i^3 \left[\text{real}(t_i(a_1, c_1, B)) - \tau_i\right]^2 \tag{6.10}$$

With this, the convergence problems experienced previously ceased, and in all cases the miminization procedure found the correct parameters for the reconstruction of

the initial profile. An illustration of the performance of the method with a large selection of different profiles is shown in 6.7.

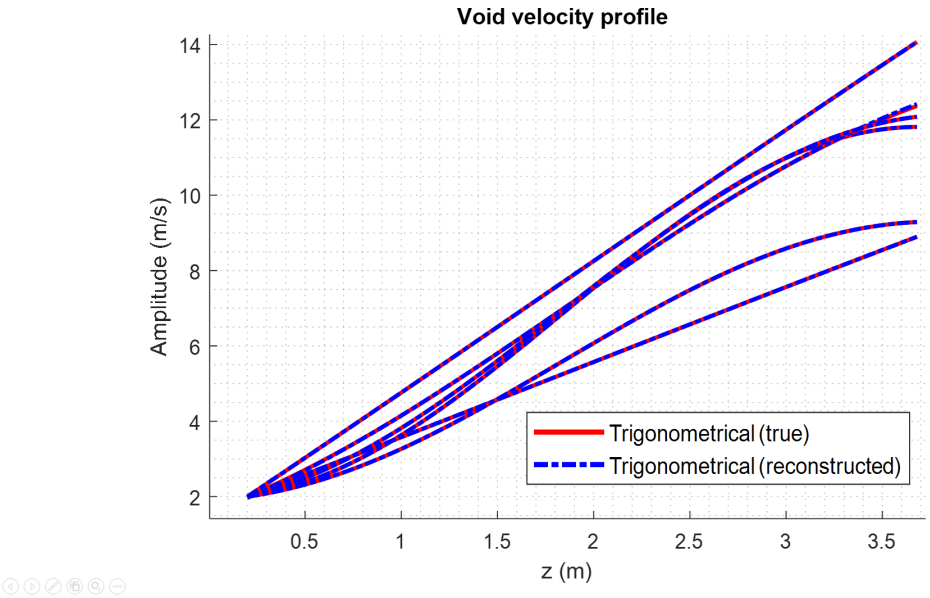

Figure 6.7: Reconstruction of several different trigonometric velocity profiles

6.5.2 Polynomial profile

For the tests with the polynomial profile, the form (6.2) was used. This form has four fitting parameters. It was tested in two different ways. First, we assumed that the correct axial position h of the onset of boiling is known (e.g. from a tip measurement). In that case, there are only the three parameters b, c and d to be fitted. Second, we assumed that the correct value of h is not known, rather it was guessed incorrectly, with a certain error. The interesting question was then to see how large an error this incorrect estimate causes in the reconstruction process.

Reconstruction with a known boiling onset point h

In this case the unfolding worked always correctly and promptly, without the need of taking the real value of the penalty function. Finding correct initial values of the parameters for the minimisation process was easy, by taking a qualified guess of the void velocity at the outlet, the velocity gradient at the axial position of the inflection point of the profile and the void velocity at the position of the second detector. It seamed that handling the polynomial profile was more efficient than that of the trigonometric profile. One case of a successful reconstruction is shown in Fig. 6.8, where the following data were used:

$$\text{H} = 3.68 \text{ m}; \qquad \text{h} = 0.2 \text{ m}; \qquad v_0 = 2 \text{ m/s}; \qquad v(z = H) = 12.1 \text{ m/s}.$$

It is seen in Fig. 6.8 that the reconstruction is completely successful.

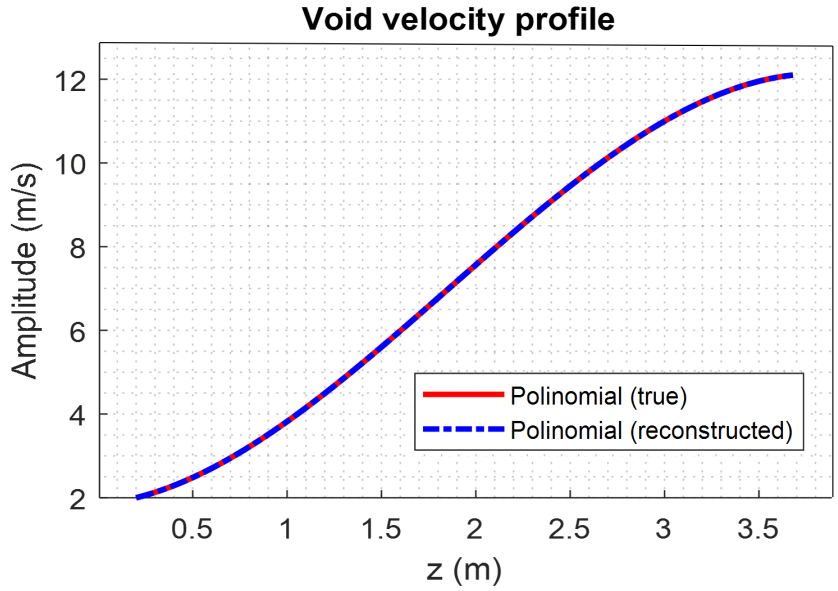

Figure 6.8: Reconstruction of a polynomial velocity profile.

Reconstruction with an unknown boiling onset point h

In this case we assumed a value for the onset point in the reconstruction procedure which was different from the true one. In a practical case, when no information on the boiling onset point is available, it is a reasonable choice to assume the position at the boiling onset halfway between the core inlet and the position of the lowermost detector, because this miminizes the error of the guess. Since the lowermost detector position is at 0.66 m, we selected $h = 0.33$ m. Two reconstructions were made, one by taking $h = 0.45$ m for the true onset point, and another by taking $h = 0.15$ m for the true onset point.

The results of the reconstruction are seen in Fig. 6.9. It is seen that, as expected, the reconstruction will not be perfect, especially in the lower section of the core. However, as it is also seen in the figure, the only difference between the true and the reconstructed profiles is at the lowermost part of the core, and the incorrect reconstruction affects slightly only the velocity at the position of the lowermost detector. The rest of the profiles, hence also the velocities at the other three detector positions, are all correct.

6.5.3 Significance of choosing the right type of profile

One might also be interested to know the significance of choosing the right type of profile. In other words, to check the performance of the reconstruction procedure when the true profile is trigonometric, and the reconstruction is attempted by using a polynomial form, and vice versa.

The results of such a test are shown in Fig. 6.10. In the left hand side figure the true profile is trigonometric, whereas the reconstruction is made by the assumption

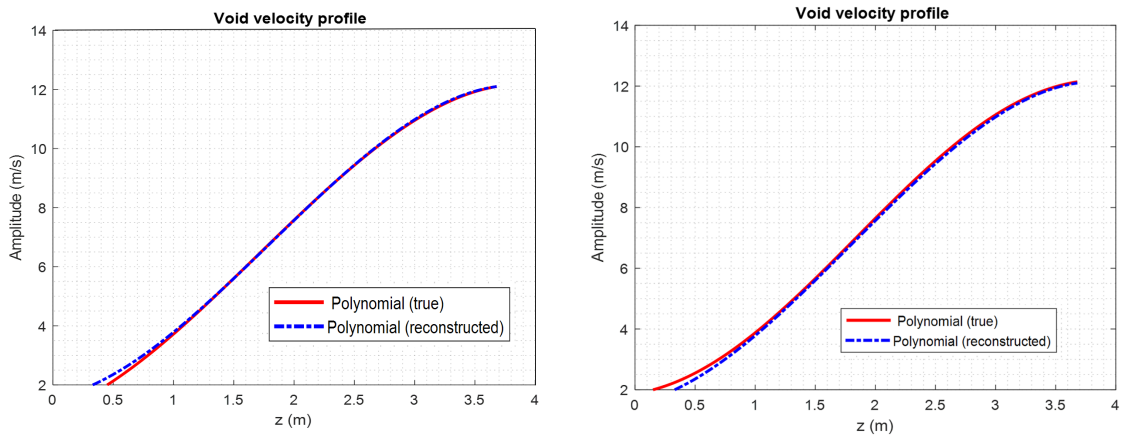

Figure 6.9: Left figure: trigonometric profile (true) reconstructed by assuming a polynomial profile; right figure: polynomial profile (true) reconstructed by assuming a trigonometric profile.

of a polynomial form. In the right hand side figure the opposite case is shown, i.e. when the true profile is polynomial, whereas the reconstruction is made by the assumption of a trigonometric form.

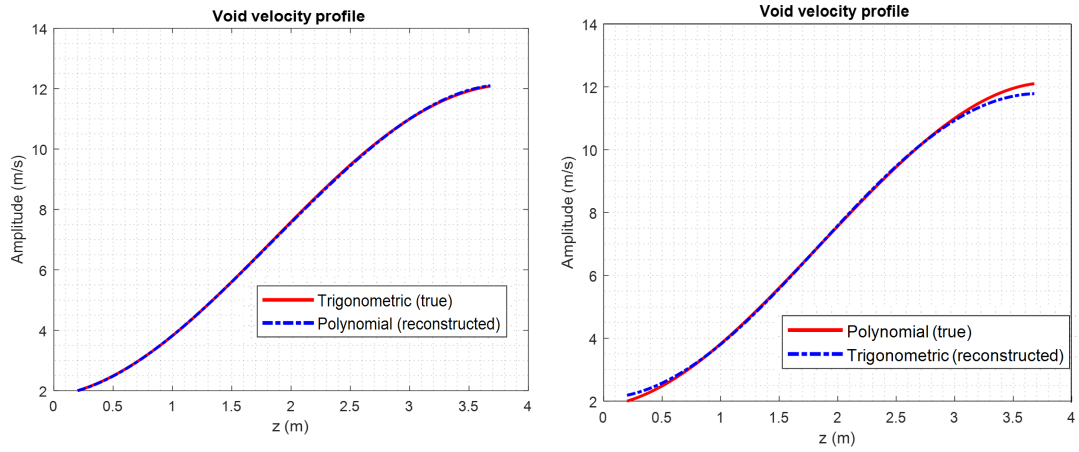

Figure 6.10: Reconstruction of two polynomial velocity profiles with uncorrect values of the boiling onset point h in the reconstruction algorithm. The guessed value is $h = 0.33$ m in both cases. Left hand side figure: true value $h = 0.45$ m; right hand figure: true value is $h = 0.15$ m.

It is seen that the use of the polynomial profile is more flexible than that of the trigonometric profile. It can very well reconstruct a true trigonometric profile throughout the whole axial range. It has though to be added, that here it was assumed that the onset point of the boiling is known. The figure also shows that when the true profile is polynomial, the trigonometric form has a slight error in the reconstruction both at low and at high elevations.

The overall conclusion of these model tests is that use of the polynomil profile is preferred to be used in the reconstruction over the simpler trigonometric profile.

6.6 Test with Ringhals-1 data

It might be interesting to test the procedure with pure measurement data, where the true values of the flow profile parameters are not known. This has the disadvantage, that in such a case the validity of the reconstructed velocity profile cannot be verified, but it is a test of whether the unfolding procedure works when one cannot give a qualified guess of the starting values for the search of the minimum. To this end we took real measurement data from Ringhals-1 [10]. These are given below in Table 6.1.

Table 6.1: **Transit times from Ringhals-1 (from [10])**

τ_1 [s]	τ_2 [s]	τ_3 [s]
0.2712	0.2111	0.1253

Since in this case neither the true character of the profile, nor the values of the corresponding parameters are known, the only assurance of the successful reconstruction is that the reconstructed values at least reproduce the transit times properly. One could expect that the task is underdetermined, i.e. that several void velocity profiles may can be constructed which all reproduce the proper transit times, but are otherwise different, and supply therefor different values for the velocities at the detector positions.

Both the trigonometric and the polynomial forms were used in the attempt of reconstructing the velocity profile. It was expected that the reconstructed profile looks like in most of the figures, in particular as in Figs 6.2 and 6.3, i.e. with a distinct inflection point. To some surprise, it turned out that the profiles, either trigonometric or polynomial, which were able to reconstruct the measured transit times, resembled much more to the TRACE simulations in Fig. 6.1. The reconstructed profile, which yielded the best agreement with the measured transit times, is shown in Fig. 6.11.

When comparing the performance of the two methods, i.e. the trigonometric vs the polynomial profile, it was once again found that assumption of the polynomial profile in the reconstruction performed better. This is because it has more free parameters that can be fitted, and hence this model is more flexible. Finding the proper parameter values which must be fixed for the search for the minimum of the penalty function took more trial and error, but also it made possible to find a better fit in the end.

Thus it turned out that the original concern that the case is underdetermined and one may obtain multiple solutions, was not valid for this case. This is not a proof that this should be the case in all other measurements, but at least it is reassuring. Significantly more cases need to be investigated to get a confirmation of the validity of the procedure, and validation against calculated or measured values is desired.

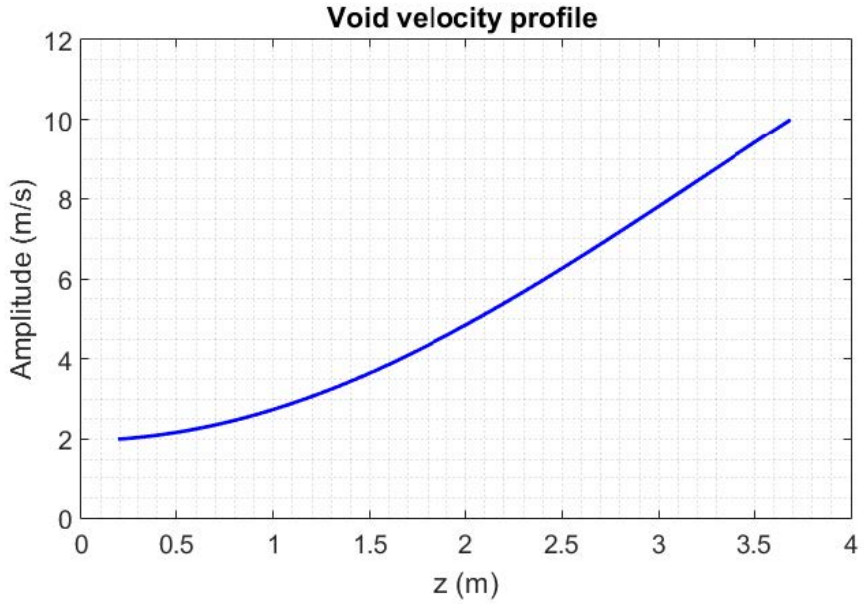

Figure 6.11: Void velocity profile obtained from Ringhals measurements

6.7 Conclusions

The results obtained by both simulations and from a single application to a real case are promising, but further work is required in several areas. There is a thorough need for verification of the method, which in turn requires access to realistic void velocity profiles. One possibility is to produce high-fidelity realistic void velocity profiles generated by system codes, for various reactor types and fuel cycles. In such calculations the true functional form of the profile for a given reactor construction could be established. Another possibility is to get access to measurement data. These could be obtained either from dedicated measurements in critical assemblies or research reactors, or, more likely, from instrumented fuel assemblies at operating BWRs, such as all three Forsmark reactors, or Oskarshamn 3. Yet another possibility is to use the extensive data base, represented by the noise measurements made in all Swedish power reactors by GSE Power Systems, which is available from SSM [30]. Finally, the model introduced in this work could be extended to depend on four parameters, such that it can describe more complicated profiles than those shown here.

7. PROPOSAL FOR 2020-21

1. Analysis of vibrations of thimble tubes with axially dependent in-core measurements in various radial positions.

2. Evaluation of new ex-core measurements for beam, reactivity, shell and tilting mode vibrations in R3 or R4.

3. Further experimental work and simulations to evaluate the feasibility of using fission chambers in the current mode for reactor diagnostics, as an alternative of pulse counting methods. In particular, for reactivity measurements, the current-based form of the Feynman-alpha method will be tested.

4. Further development of a new method to determine the axial velocity profile of the void in the core of a BWR by using four permanent in-core LPRMs and a TIP detector. This could include evaluations of previous noise measurements, made originally for other purposes by GSE Power Systems AB during 1985-1995 in several Swedish BWRs.

8. ACKNOWLEDGEMENT

This one-year contract was performed by funding from Ringhals Vattenfall AB, contract No. 686103-003. Contact person from Ringhals was Dr. Henrik Nylén.

REFERENCES

[1] F. Zylbersztejn, H. N. Tran, I. Pázsit, P. Filliatre, and C. Jammes, "Calculation of the neutron noise induced by periodic deformations of a large sodium-cooled fast reactor core," *Nucl. Sci. Engng*, vol. 177, pp. 203–218, 2014.

[2] I. Pázsit (Ed.), "*Final Report on the Research Project Ringhals Diagnostics and Monitoring, Stage 1*," CTH-RF-122/RR-3, Chalmers University of Technology, Göteborg, Sweden, September 1996.

[3] I. Pázsit, J. Karlsson, and N. Garis, "*Final Report on the Research Project Ringhals Diagnostics and Monitoring, Stage 2*," CTH-RF-132/RR-4, Chalmers University of Technology, Göteborg, Sweden, October 1997.

[4] J. K.-H. Karlsson and I. Pázsit, "*Final Report on the Research Project Ringhals Diagnostics and Monitoring, Stage 3: Analysis of core barrel vibrations in Ringhals 2, 3 and 4 for several fuel cycles*," CTH-RF-135/RR-5, Chalmers University of Technology, Göteborg, Sweden, October 1998.

[5] M. Pázsit and I. Pázsit, "*Final Report on the Analysis of Core Barrel Vibrations in Ringhals PWRs R2, R3 and R4 from Measurements Made in 2005*," Internal report, Chalmers University of Technology, Göteborg, Sweden, 2006.

[6] C. Sunde, C. Demazière, and I. Pázsit, "*Final Report on the Research Project Ringhals Diagnostics and Monitoring, Stage 11*," CTH-NT-206/RR-13, Chalmers University of Technology, Göteborg, Sweden, February 2007.

[7] I. Pázsit, C. Demazière, C. Sunde, P. Bernitt, and A. Hernández-Solís, "*Final Report on the Research Project Ringhals Diagnostics and Monitoring, Stage 12*," CTH-NT-220/RR-14, Chalmers University of Technology, Göteborg, Sweden, August 2008.

[8] I. Pázsit, C. Montalvo Martín, V. Dykin, and T. Tambouratzis, "*Final Report on the Research Project Ringhals Diagnostics and Monitoring, Stage 13*," CTH-NT-230/RR-15, Chalmers University of Technology, Göteborg, Sweden, March 2010.

[9] I. Pázsit, C. Montalvo Martín, V. Dykin, and H. Nylén, "*Final Report on the Research Project Ringhals Diagnostics and Monitoring, Stage 14*," CTH-NT-253/RR-16, Chalmers University of Technology, Göteborg, Sweden, December 2011.

[10] V. Dykin, C. Montalvo Martín, H. Nylén, and I. Pázsit, "*Ringhals Diagnostics and Monitoring, Final Research Report 2012 - 2014*," CTH-NT-304/RR-19, Chalmers University of Technology, Göteborg, Sweden, December 2014.

[11] V. Dykin, C. Montalvo, N. Tran, H. Nylén, and I. Pázsit, "*Ringhals Diagnostics and Monitoring, Annual Research Report 2015*," CTH-NT-319/RR-20, Chalmers University of Technology, Göteborg, Sweden, December 2015.

[12] I. Pázsit, C. Montalvo, N. Tran, H. Nylén, and O. Olvera Guerrero, "*Ringhals Diagnostics and Monitoring, Annual Research Report 2016-17*," CTH-NT-333/RR-21, Chalmers University of Technology, Göteborg, Sweden, December 2017.

[13] I. Pázsit, L. A. Torres, C. Montalvo, Y. Kitamura, L. Nagy, and H. Nylén, "*Ringhals Diagnostics and Monitoring, Annual Research Report 2018-19*," CTH-NT-333/RR-21, Chalmers University of Technology, Göteborg, Sweden, June 2019.

[14] M. Nilsson, "*Brusmätning för att söka lågfrekventa störningar i R3, Annual Research Report 2015*," Ringhals internal report UH-rapport 2099930 / 2.0, Ringhals AB, Göteborg, Sweden, October 2010.

[15] B. Severinsson, "*"Brusmätningar för analys av härdhöljesvibrationer på Ringhals 3. Utförda mellan 2013-02-26 och 2013-07-05*," Ringhals internal report UH-rapport 2245846 / 2.0, Ringhals AB, Göteborg, Sweden, July 2013.

[16] B. Severinsson, "*Brusmätning för analys av Härdhöljesvibrationer på utförda under 2013*," Ringhals internal report UH-rapport 2233461 / 2.0, Ringhals AB, Göteborg, Sweden, July 2013.

[17] L. Pál, I. Pázsit, and Zs. Elter, "Comments on the stochastic characteristics of fission chamber signals," *Nuclear Instruments and Methods in Physics Research Section A: Accelerators, Spectrometers, Detectors and Associated Equipment*, vol. 763, no. 0, pp. 44–52, 2014.

[18] P. Cheol Ho ed., "Experimental Benchmarks for Accelerator-Driven System (ADS) at Kyoto University Critical Assembly," Technical report, Research Reactor Institute, Kyoto University, 2012. KURRI-TR-444.

[19] G. Klujber, I. Barth, and M. Szieberth, "*Construction of a measurement system for the data acquisition of fission chambers in the current mode*. In Hungarian (*Mérőrendszer kiépítése hasadási kamrák árammódú adatfelvételéhez)*," Technical report, Budapest University of Technology and Economics, Institute of Nuclear Techniques, 2019. BME-NTI-887/2019.

[20] StemLabs, *Red Pitaya STEMlab Board Specifications*, 2018. https://www.redpitaya.com/f130/red-pitaya-stemlab-board/.

[21] Red Pitaya StemLab, *Red Pitaya Documentation*, 2017. Revision b1890399; https://redpitaya.readthedocs.io/en/latest/.

[22] G. Klujber and M. Szieberth, "Development of FPGA based time-stamp mode data acquisition system," Technical report, Budapest University of Technology and Economics, Institute of Nuclear Techniques, 2017. BME-NTI-821/2017.

[23] I. Pázsit and L. Pál, *Neutron Fluctuations: a Treatise on the Physics of Branching Processes*. New York: Elsevier, 2008.

[24] L. Pál and I. Pázsit, "Campbelling-type theory of fission chamber signals generated by neutron chains in a multiplying medium," *Nuclear Instruments and Methods in Physics Research Section A: Accelerators, Spectrometers, Detectors and Associated Equipment*, vol. **794**, no. 1, pp. 90–101, 2015.

[25] G. Kosály, L. Maróti, and L. Meskó, "A simple space dependent theory of the neutron noise in a boiling water reactor," *Annals of Nuclear Energy*, vol. 2, no. 2, pp. 315–321, 1975.

[26] G. Kosály, "Noise investigations in boiling-water and pressurized-water reactors," *Prog. nucl. Energy*, vol. 5, pp. 145–199, 1980.

[27] V. Dykin and I. Pázsit, "Simulation of in-core neutron noise measurements for axial void profile reconstruction in boiling water reactors," *Nuclear Technology*, vol. 183, no. 3, pp. 354–366, 2013.

[28] I. Pázsit and C. Demazière, *Noise Techniques in Nuclear Systems*, vol. 2 of *Handbook of Nuclear Engineering*, pp. 1631 – 1737. Springer Science, 2010.

[29] "Wolfram Research, Inc., Mathematica, Version 12.0.0.0." Champaign, IL., 2019.

[30] B. G. Bergdahl, "Brusdata-bibliotek - Data från mätningar och experiment under åren 1985-1995 konverterade från band till CD," SSM report, GSE Power Systems AB, 2002. SKI Rapport 02:6.

CHALMERS UNIVERSITY OF TECHNOLOGY
SE 412 96 Gothenburg, Sweden
Phone: + 46 - (0)31 772 10 00
Web: www.chalmers.se